Revista Brasileira de Ciência do Solo

Division - Soil Processes and Properties | Commission – Soil Physics

Inversion of soil moisture and its feedback on ecological restoration in arid and semi-arid areas of northwest China

Xin Liu[1], Yuanyuan Hao[1]*, Ziyan Zhou[1], Limin Hua[1], Wenxia Cao[1], Ruifang Zhang[1], Xin Yang[1] and Tao Yu[1]

[1] College of Grassland Science, Gansu Agricultural University, Key Laboratory of Grassland Ecosystem of the Ministry of Education, Engineering and Technology Research Center for Alpine Rodent Pests Control, National Forestry and Grassland Administration, Lanzhou 730070, China.

*** Corresponding author:**
E-mail: haoyy@gsau.edu.cn

Received: August 26, 2022

Approved: November 03, 2022

How to cite: Liu X, Hao Y, Zhou Z, Hua L, Cao W, Zhang R, Yang X, Yu T. Inversion of soil moisture and its feedback on ecological restoration in arid and semi-arid areas of northwest China. Rev Bras Cienc Solo. 2022;46:e0220113.
https://doi.org/10.36783/18069657rbcs20220113

Editors: José Miguel Reichert and Milton César Costa Campos.

ABSTRACT: Soil moisture (*SM*) plays an important role in regulating the global water cycle, especially in arid areas, and is one of the main indicators of ecological environmental health. Although traditional methods can accurately measure *SM* at a single sample site, they are limited in large-scale and dynamic *SM* monitoring. Therefore, we used the Landsat images as the data source and the soil adjusted vegetation index (*SAVI*) to build the adjusted *SAVI* (*aSAVI*) index by modifying the soil adjustment parameter *L* and introducing the short-wave infrared band. According to the theory of temperature vegetation dryness index (*TVDI*) and feature space, we introduced a model, combined the measured *SM* data (Minqin Basin, China) through a comparative analysis of four vegetation indices (*NDVI, SAVI, MSAVI, aSAVI*) determine the optimal model. Taking the Minqin Basin as the study area, the spatiotemporal variation characteristics of *SM* in three sub-regions (the entire study area, irrigated region, and periphery of the irrigated regions) were quantitatively analyzed and compared in four different periods: *pre*-Comprehensive Treatment Program of the Shiyang River Basin (*pre-CTSRB*) (2000–2005), *CTSRB I* (2006–2010), *CTSRB II* (2011–2016), and *CTSRB-end* (2017–2021) to evaluate the ecological restoration effects of treatment programs from the *SM* perspective. The results showed that: 1) *SM* values derived from *TVDI* inversion and the *aSAVI* were more accurate, and the model sensitivity decreased with soil depth; 2) the mean value of *SM* fluctuated across the four periods but decreased slightly over the entire time series. The spatial variations of the *SM* were characterized by a “descending then ascending” trend. Soil moisture increased in 21.35 % of areas at 0.00-0.10 m in the past 22 years, and 59.66 % at 0.10-0.20 m. There was a negative correlation between the mean variation trend of *SM* and the percentage of area where *SM* fell in different periods; 3) the treatment program positively affected the ecological restoration of the Minqin Basin from the *SM* perspective. The area where *SM* increased was larger than that of decreasing *SM*, especially in 0.10-0.20 m soil layer. The increase can promote growth and confer resistance to desertification.

Keywords: soil moisture, adjusted *SAVI* (*aSAVI*), time series, arid / semi-arid regions, ecological restoration project.

INTRODUCTION

Soil is the interface that connects the biosphere and atmosphere, and water cycle process of the earth's ecological environment (Zhang et al., 2018). Soil moisture (*SM*) is a control variable in the heat and water exchange cycle between the land surface and atmosphere; it affects precipitation and evapotranspiration in different meteorological environments (Seneviratne et al., 2010) and can directly characterize the wet and dry conditions of the surface environment (Wang et al., 2018). Soil moisture also plays a regulatory role in the water cycle (Mulder et al., 2011), while the water content of different soil types affects the terrestrial water cycle; for example, the water storage capacity of loam is much higher than that of sandy soil (Assi et al., 2018). If the proportion of clay is too small, there will be great restrictions on agricultural development (Wells et al., 2022). Soil moisture can affect the moisture content of organisms (vegetation, microorganisms, etc.) (Liancourt et al., 2012) and is the basic variable for agricultural production development, making it an indispensable part of the balance of the ecological environment. Therefore, understanding *SM* variation is a prerequisite for studying the complex relationships among climate, hydrology, and biology (vegetation) from multiple perspectives.

Soil moisture is essential for vegetation, but it is difficult to reliably determine this variable using direct measurements (Seneviratne et al., 2010). Generally, traditional methods are time and cost-consuming, as they can be used for only a limited number of samples (Charlton, 2000). In addition, due to the existence of various uncertain influencing factors, such as soil type, groundwater distribution, and topographical changes, the spatial variability of soil is complex (Holzman et al., 2014). Therefore, the method of monitoring *SM* in a certain area based on the actual measurement of sample points has limitations regarding the accuracy and temporality of the monitoring results (Hamidisepehr et al., 2017; Xie et al., 2017).

Based on this background, we attempted to combine remote sensing technology with the *SM* monitoring method. Since the 1980s, various vegetation index (*VI*) based on remote sensing data have been used to invert and monitor *SM*, starting with the normalized differential *VI* (*NDVI*) and land surface temperature (*LST*) (Carlson et al., 1981; Sucksdorff and Ottle, 1990). We considered this as a starting point to conduct continuous in-depth research. At present, the inversion of *SM* has achieved considerable progress in both microwave and optical remote sensing (Wigneron et al., 1995; Zhao et al., 2016). Microwave remote sensing mainly uses the relationship between short radiation bands and radar backscattering coefficients to retrieve *SM* (Jackson et al., 2012; Periasamy and Shanmugam, 2017). Using various bands or spectra to construct an index to simulate *SM* is a common method for optical remote sensing, and the main methods include *TVDI*, apparent thermal inertia (*ATI*), thermal infrared remote sensing, reflectance, and the model with temporal and spatial heterogeneity. The reflectance method is simple and quick to operate, but it is only suitable for areas with flat terrain and single landforms (Zhang et al., 2017). The difference in sensors limits the albedo calculation in *ATI*, and generally, the effect is better in the early stages of vegetation growth (Sun et al., 2015). The *TVDI* can effectively overcome the influence of soil background and achieve better results in areas with incomplete coverage (Chen et al., 2011).

Based on the above-mentioned reasons, scholars focused on the *TVDI* and found that the relationship between the relative changes in *VI*, *LST*, and *SM* was relatively stable under most climatic conditions and surface cover conditions (Carlson et al., 1990). The triangular or trapezoidal two-dimensional feature space formed by *LST* and *NDVI* (Liu et al., 2021a) was used to estimate the *TVDI*. The upper and lower thresholds of land surface temperature are represented on both sides of the characteristic space, and the calculated *TVDI* values are subsequently used to infer the degree of drought, which can more accurately determine the *SM*. A significant negative correlation was found between the *TVDI* and *SM* in different arid and semi-arid regions (Guo et al., 2009;

Kazemzadeh et al., 2021). Due to the discrepancies in climate and soil environment in different regions, the feature space (*Vis-TVDI*) and *LST* that constitute the *TVDI* were modified in a suitable manner, summarized as follows: (a) replaced *NDVI* and used the modified soil adjusted *VI* (*MSAVI*), soil adjusted *VI* (*SAVI*), and enhanced *VI* (*EVI*) for evaluation (Zhang et al., 2014a; Ma et al., 2017; Wu et al., 2019); (b) modified the soil line and increased the combination of shortwave infrared (*SWIR*), near-infrared (*NIR*), and red light bands to reduce the sensitivity of *VI* to the soil background (Feng et al., 2011a; Chen et al., 2019; Liu et al., 2021b); (c) considered the influence of factors such as terrain (digital elevation model, *DEM*) and environmental data on the *LST* and made corrections to the *LST* (Ran et al., 2005; Sun et al., 2010; Liu et al., 2013). The correlation between the *TVDI* and *SM* obtained after the modification was clear, which improved the accuracy of *SM* inversion (Thi et al., 2019; Yan et al., 2019). However, the above results were only a single-factor modification, and the influence of factors such as *VI*, *SWIR* band, and altitude on the accuracy of the *TVDI-SM* model was not comprehensively discussed. Furthermore, the inversion of *SM* is often only a distribution model, and little attention has been paid to the practical application of the model and the establishment of relevant evaluation mechanisms.

To find an optimal model for *SM* in arid and semi-arid areas of northwest China, in this study, we established the *TVDI* after revising *VI* and *LST*, and constructed a model between *TVDI* and *SM* to explore its ecological impacts. In addition, to better understand the key process of *SM* changes over time in arid and semi-arid regions, we carried out analysis in combination with time series. We used our model to obtain the *SM* distribution in the study area from 2000 to 2021 and to evaluate the different periods (before, during, and after) of the ecological restoration project to determine whether change in *SM* promoted ecological restoration. Our model will provide a framework for the comprehensive management of *SM* sustainability in arid and semi-arid areas and directions and references for ecological restoration, and affect evaluation research from the perspective of *SM*.

MATERIALS AND METHODS

Study area

The study area was in the Minqin county in Gansu Province, northwestern China, downstream of the Shiyang River Basin in the northeast of the Hexi Corridor, and between the Badain Jaran and Tengger Deserts (Figure 1). This area has important reference value for China's desertification control research and ecological environment restoration construction (Ma et al., 2013). The altitude is between 1190 to 1465 m, and the main landforms are deserts, low hills, and plains. The soil type is Arenosols (IUSS Working Group WRB, 2015), but the continuous erosion of the two deserts and the development of unscientific irrigated agriculture have led to desertification, salinization, and degradation of the soil (Ren et al., 2014).

The studied area has a temperate continental arid climate, with four distinct seasons. It is windy in winter and spring and hot in the summer. The temperature can vary greatly daily, with frequent sandstorms and extreme imbalances between precipitation and evaporation. Specifically, the annual average precipitation (114 mm) is only approximately 4.55 % of the annual average evaporation (2483 mm). The average annual temperature is 38.4 °C, with an average annual wind speed is 2.7 m s^{-1}. To distinguish the oasis in the basin and its periphery, the study area was divided into the irrigation area and the periphery of the irrigation area. Crops make up most of the vegetation in the irrigation area, while the periphery of the irrigation area is dominated by halophytic and xerophytic vegetation. The main crops are wheat and corn; the wild vegetation includes woody plants, such as shrubs and subshrubs, which are more common, as well as annual and perennial herbs. Among them, shrubs are mainly *Kalidium foliatum* (Pall.) Moq., *Nitraria* *tangutorum* Bobr., and *Reaumuria songarica* (Pall.) Maxim., and herbaceous plants include *Peganum harmala* L., *Phragmites australis* (Cav.) Trin. ex Steud., and *Suaeda glauc*a (Bunge) Bunge.

Currently, the studied area mainly consists of irrigated agriculture, but unscientific irrigation (surface flooding irrigation, uncontrolled groundwater extraction) methods before 2006 caused irreversible damage to the ecological environment of the area. The main problems caused were: (a) continuous groundwater level decline and soil desertification intensified; (b) merging of the two deserts; (c) different degrees of ecological degradation, reflected in soil, vegetation, groundwater, and other aspects (Zhang et al., 2004). To curb the continuous decline of the groundwater level in the Minqin oasis and restore the ecological environment of Minqin, and the entire Shiyang River basin, the Chinese government launched the Comprehensive Treatment Program of the Shiyang River Basin (*CTSRB*) in January 2006. Increasing surface runoff and reducing groundwater extraction were two major treatment measures of the *CTSRB* (Hao et al., 2017). The project was implemented in two periods: *CTSRB I* (2006–2010) and *CTSRB II* (2011–2020; however, it was completed in 2016). Therefore, different time nodes of project implementation were used to divide the time stages in the study. The project preparation period from 2000 to 2005 (*pre-CTSRB*), the first period from 2006 to 2010 (*CTSRB I*), the second period from 2011 to 2016 (*CTSRB II*), and the end period from 2017 to 2021 (*CTSRB-end*) were used. The spatiotemporal variations of *SM* were analyzed in four periods to evaluate the ecological restoration effect of the *CTSRB* from the perspective of *SM*.

Data

In situ SM

Farmland abandoned for ecological restoration from 2006 to 2010 in the *CTSRB* was selected to meet the requirements of the surrounding area with closed irrigation wells and was converted to ecological restoration land. To improve the accuracy of the inversion and avoid subjective errors, the sampling points of the experiment were selected in ecological restoration land where the vegetation grows evenly and is less affected by human activities, which also makes the soil samples more representative.

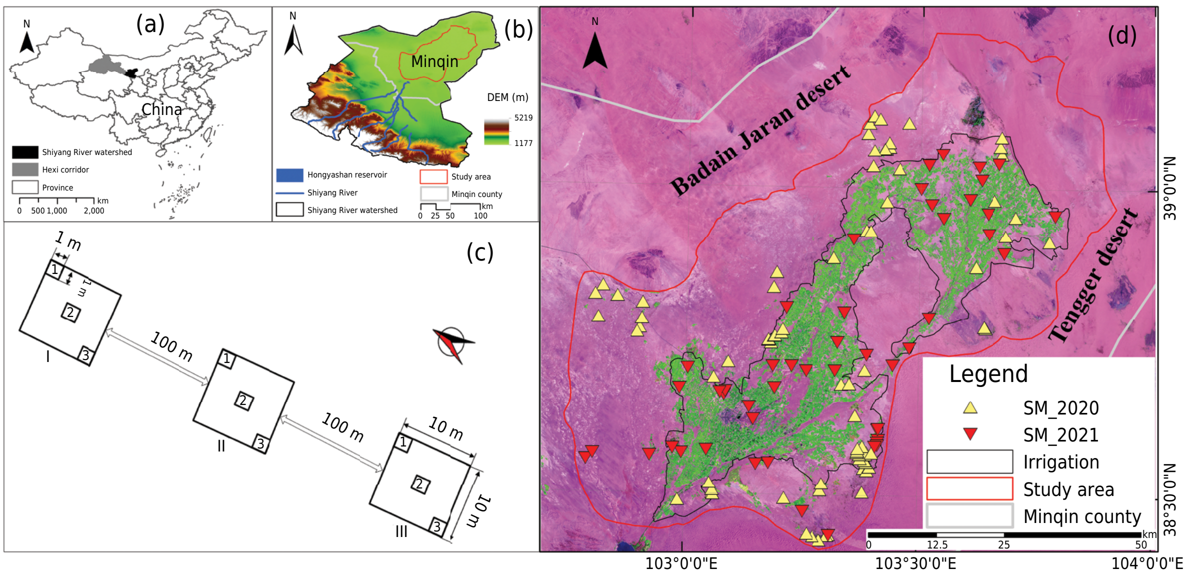

Figure 1. Studied area location and distribution of *SM* sampling points. (a) location of the Hexi Corridor and Shiyang River Basin in China; (b) location of the studied area in Shiyang River Basin; (c) soil sample collection method; (d) distribution of sampling points in the study area.

Data were collected from field samples taken in the study area in July 2020 and 2021 and were brought back to the laboratory for *SM* measurements. A total of 130 points (2020, 79 points; 2021, 51 points) were sampled (Figure 1). The specific sampling method was as follows: at each sampling point, three large sample squares of 10 × 10 m were arranged at 100 m intervals in the north-south direction. In each large sample square, three samples were taken on the north-south diagonal and recorded as a repetition (Cosh et al., 2013). At each point, the soil samples were taken at three soil layers (0.00-0.10, 0.10-0.20, and 0.20-0.30 m) using the ring knife method (Xu et al., 2022), and the latitude and longitude coordinates and surrounding environment information were recorded (Figure 1c) (McAlary et al., 2009; Sousa et al., 2022). Soil moisture was obtained using the soil drying method (Wong et al., 2020).

Remote sensing data

Landsat remote sensing images (collection1-L1 level) were obtained from the USGS (United States Geological Survey, 2021), and we chose July or August (vegetation grows vigorously or reaches the flowering period) in 2000–2021 (Path/Row is 131/033, 132/033). The spatial resolution of the multi-spectral bands was 30 m and the thermal infrared bands were 100 m (TM and TIRS) and 60 m (ETM+). According to the orbital repetition period (16 days) and cloud cover, the images that affected the inversion result were eliminated. The best images from each year were screened according to the satellite revisit period and cloud distribution. Specific image information is presented in table 1. Image preprocessing was completed using ENVI software, including radiometric calibration, FLAASH atmospheric correction, resampling, geometric correction, image mosaic, cropping, and band calculation. On 31 May, 2003, the Scan Line Corrector (*SLC*) onboard the Landsat 7 ETM+ satellite failed, which caused approximately 22 % of the striped data to be lost in the images acquired subsequently. The *SLC*-off model was used for correction.

To rule out the influence of precipitation on the selected remote sensing images, and to verify whether they are representative, the precipitation of the 5 days before, 10 days before and 15 days before of the annual images between 2000 and 2021 was

Table 1. Details of Landsat data usage

Year	Sensor	Path/Row	Date	Cloud	Quality	Year	Sensor	Path/Row	Date	Cloud	Quality
2000	TM	131/033	2000.07.19	0.00 %	9	2014	OLI/TIRS	131/033	2014.07.26	0.00 %	9
2001	TM	131/033	2001.07.22	0.00 %	9			132/033	2014.07.17	0.00 %	9
2002	ETM+	131/033	2002.07.17	3.00 %	9	2015	OLI/TIRS	131/033	2015.07.29	2.77 %	9
2003	TM	131/033	2003.08.13	3.00 %	7			132/033	2015.08.05	3.02 %	9
2004	TM	131/033	2004.07.30	0.00 %	7	2016	OLI/TIRS	131/033	2016.07.15	0.30 %	9
2005	TM	131/033	2005.08.02	0.00 %	7			132/033	2016.07.06	2.68 %	9
2006	TM	131/033	2006.07.04	0.00 %	9	2017	OLI/TIRS	131/033	2017.07.18	0.95 %	9
2007	ETM+	131/033	2007.07.15	0.00 %	9			132/033	2017.07.09	2.55 %	9
2008	TM	131/033	2008.07.25	0.00 %	7	2018	OLI/TIRS	131/033	2018.07.21	0.47 %	9
2009	TM	132/033	2009.08.13	4.00 %	9			132/033	2018.07.12	0.16 %	9
2010	ETM+	131/033	2010.07.23	2.00 %	9	2019	OLI/TIRS	131/033	2019.07.24	**22.02 %**	9
2011	ETM+	131/033	2011.07.26	0.00 %	9			132/033	2019.07.31	3.02 %	9
2012	ETM+	131/033	2012.08.29	0.00 %	9	2020	OLI/TIRS	131/033	2020.07.26	4.72 %	9
2013	OLI/TIRS	131/033	2013.08.08	4.74 %	9			132/033	2020.07.17	**14.72 %**	9
		132/033	2013.07.30	**14.48 %**	9	2021	OLI/TIRS	131/033	2021.07.13	0.03 %	9
								132/033	2021.07.20	0.01 %	9

counted. In figure 2, except for the selected remote sensing images in 2004, which had more precipitation (>40 mm), the precipitation of the selected remote sensing images in other years was below 30 mm, and most of them were less than 10 mm. The precipitation in the study area decreased throughout the period prior to image capture, and the area experienced a temperate desert climate from July to August (with the high temperature during the day). With these temperatures and insufficient (≤30 mm) precipitation (5 days before), the selected images are representative of the ecological environment of the studied area in that year and can therefore be used for subsequent inversion research.

DEM data

Digital elevation model from the Resources and Environment Science Center of the Chinese Academy of Sciences (2003), with a resolution of 30 m. ArcGIS 10.3 and ENVI 5.3 were used for processing.

Methods

Acquisition of VI

Vegetation index can show vegetation information (Xiang et al., 2022). Normalized difference vegetation index is a *VI* that incorporates external factors such as illumination, surface undulation, and roughness for vegetation monitoring and is considered first in vegetation monitoring (van Leeuwen et al., 2006). We used the *SAVI*, a *VI* based on *NDVI* and a large amount of observational data proposed by Huete (1988). The *MSAVI* further weakens the influence of the soil background, replacing the constant soil adjustment index (*L*) in *SAVI* with a variable, resulting in increased sensitivity to vegetation (Qi et al., 1994). Finally, the *SAVI* was modified by adding short-wave

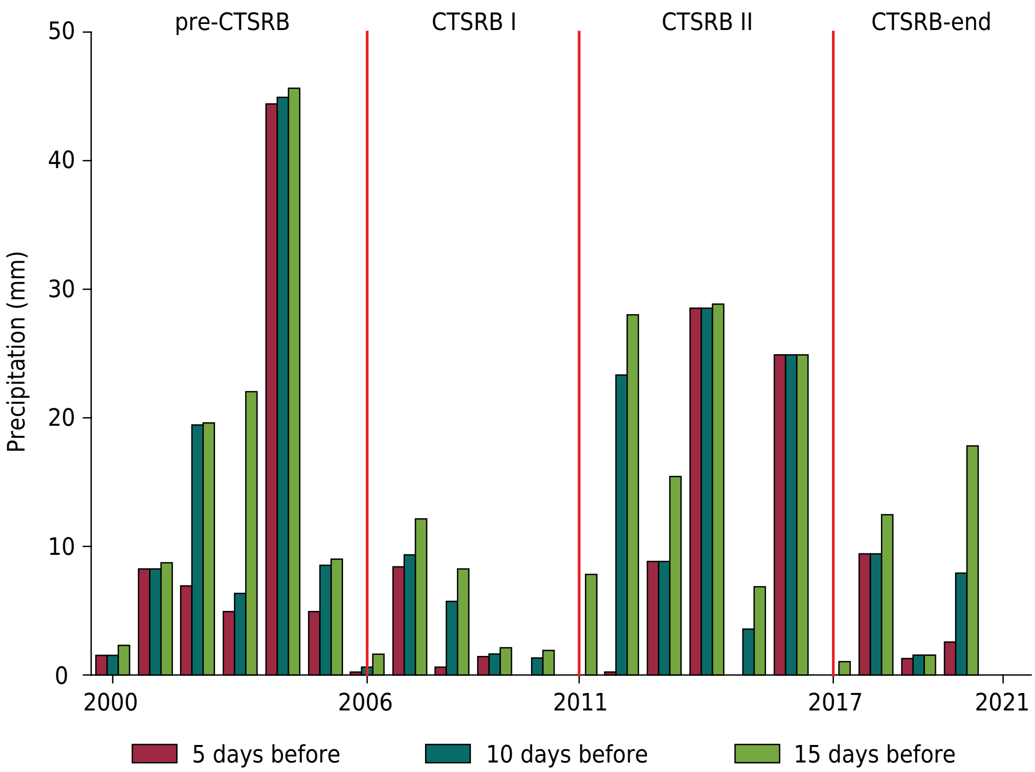

Figure 2. Pre-precipitation of selected images from 2000 to 2021 in our study area. Red, blue and green columns represent the precipitation 5, 10 and 15 days before image capture, respectively, over time.

infrared bands and modifying L to obtain the adjusted soil adjustment VI ($aSAVI$). The above four VIs were calculated as follows:

$$NDVI = \frac{(\rho_{NIR} - \rho_{Red})}{(\rho_{NIR} - \rho_{Red})} \quad \text{Eq. 1}$$

$$SAVI = (1 + L)\ \frac{(\rho_{NIR} - \rho_{Red})}{(\rho_{NIR} - \rho_{Red} + L)} \quad \text{Eq. 2}$$

$$MSAVI = \frac{2\ \rho_{NIR} + 1 - \sqrt{(2\ \rho_{NIR} + 1)^2 - 8(\rho_{NIR} - \rho_{Red})}}{2} \quad \text{Eq. 3}$$

$$aSAVI = (1 + L)\ \frac{(\rho_{NIR} - \rho_R + \rho_{SWIR}\ )}{(\ \rho_{NIR} - \rho_R + \rho_{SWIR} + L)} \quad \text{Eq. 4}$$

In which: ρ_{NIR}, ρ_{Red}, and ρ_{SWIR} are the near-infrared, red and short-wave infrared band wavelengths, respectively; L is generally 0.5; in this study, L = 0.23 in $aSAVI$ after many tests.

SAVI-aSAVI

Modify the parameters of L

SAVI is a *VI* that considers the sensitivity of the soil background and is generated by observing a large amount of vegetation and soil data. It adds a soil adjustment coefficient "*L*" on the basis of *NDVI* (Huete, 1988). However, when using the empirical value "L = 0.5", *SAVI* cannot fully explain the local vegetation information and many outliers will appear. Studies have used different approaches to modify the L value, which depends on the region being studied; however, modifying L can generally better tailor performance results to local conditions (Ma et al., 2017; Wu et al., 2019). The use of variables instead of L in the *MSAVI* to further increase the sensitivity of vegetation (Qi et al., 1994), such as the negative factor (L = -0.2) (Zhen et al., 2021) and enlarge L value (L = 100) (Kasim et al., 2018), are more appropriate for the study of vegetation coverage (*VC*) in arid and semi-arid regions, and can also alleviate the saturation of *SAVI* (Ren et al., 2018). Based on the premise that the confidence is 0.95 and meets the threshold of the *SAVI* value domain, the L value is adjusted with a step size of 0.01 from 0 to 1, reaching am optimal L value of Minqin Basin of 0.23.

Joining of SWIR band

The *SWIR* band has the characteristics of penetrating clouds, fog, and high sensitivity (Chen et al., 2019). Modified soil line and combination of *SWIR, NIR*, or Red bands can reduce *VI* sensitivity to soil background (Feng et al., 2011b; Holzman et al., 2021).

Specifically, adding *SWIR* to *VI* improved the relationship between *SAVI* and *VC* (R^2 increase 0.06) and leaf area index (R^2 increase about 0.10) (Chen et al., 2019). In complex environments, such as *VC* or bare areas, the Sentinel-2 satellite can improve the estimation accuracy of *SM* in the 0.00-0.05 m topsoil layer (R^2 increase 0.04) by combining the *SM* monitoring index with the red edge and *SWIR* band (Liu et al., 2021b). Using different high-resolution multi-spectral images, better results were obtained by estimating *SM* by *SWIR* conversion reflectivity under high spatial resolution (Feng et al., 2008). In summary, adding the *SWIR* band to the *VI* improved the inversion accuracy of *SM.* In this study, *SWIR* was added to the *SAVI* to generate the *aSAVI* model based on the best vegetation adjustment index; the adjusted *VI* was modeled and, by accuracy, verified (R^2 increased by 0.04) as more suitable for inversion of *SM* in arid and semi-arid areas.

Acquisition of VC

The pixel binary model is a common method for calculating *VC* based on a linear mixed-pixel decomposition model. The semi-empirical relationship was discovered by Gutman and Ignatov (1998*)* according to the formula proposed by Gillies and Carlson (1995). To construct a mixed pixel model, the VC is extracted from four VIs (*NDVI*, *SAVI*, *MSAVI*, and *aSAVI*). Pixels with *VI* less than 0 were excluded because they are mainly water bodies and clouds and are considered to be 100 % of *VC*. Thus, if they are, included in the calculation, the validity of the results may be affected (Yuan et al., 2020). The *VC* was calculated as follows:

$$VC = \frac{VI - VI_{min}}{VI_{max} - VI_{min}} \quad \text{Eq. 5}$$

in which *VI* is *NDVI*, *SAVI*, *MSAVI*, and *aSAVI*, and VI_{min} and VI_{max} are the maximum and minimum values of *VI*, respectively. In this study, statistical histogram analysis was conducted on each *VI*, and the maximum and minimum values were determined to be 95 and 5 % cumulative probability, respectively.

Land surface emissivity

Surface emissivity is the characterization of the ability of the land to radiate electromagnetic waves outwards and refers to the ratio of the amount of radiation emitted by the ground surface to the amount of radiation emitted by a black body at the same temperature (Zhang et al., 2014b). It not only depends on the composition of the earth's surface but also on the surface state and physical properties, and changes with the measured wavelength and observation angle (Valor and Caselles, 1996; Qin et al., 2006). It is difficult to measure the surface specific emissivity accurately and quantitatively; therefore, we divided it into water body, urban period element, natural surface, and estimates based on empirical formulae, and calculated as follows (Mallick et al., 2012; Ndossi and Avdan, 2016):

$$\varepsilon_{\text{water}} = 0.995 \quad \text{Eq. 6}$$

$$\varepsilon_{\text{urban}} = 0.9589 + 0.086 \times VC - 0.0671 \times VC^2 \quad \text{Eq. 7}$$

$$\varepsilon_{\text{surface}} = 0.9625 + 0.0614 \times VC - 0.0461 \times VC^2 \quad \text{Eq. 8}$$

$$\varepsilon = [VC<\text{''}VI_{min}\text{''}] \times \varepsilon_{\text{water}} + [\text{''}VI_{min}\text{''}<VC<\text{''}VI_{max}\text{''}] \times \varepsilon_{\text{urban}} + [VC>\text{''}\ VI_{max}\text{''}] \times \varepsilon_{\text{surface}} \quad \text{Eq. 9}$$

in which: ε is the surface emissivity.

LST

There are three common methods for *LST* inversion: thermal radiation transfer equation method, single window algorithm, and single channel algorithm (Guha et al., 2020). In this study, the thermal radiation transfer equation method was used to perform *LST* inversion in the Minqin Basin. The basic principle is to estimate the influence of the atmosphere on the surface thermal radiation, and subtract the influence of the total thermal radiation received by the satellite sensor to obtain the surface thermal radiation intensity, and finally convert the surface thermal radiation intensity into the corresponding *LST* (Chatterjee et al., 2017). This was calculated as follows:

$$L_\lambda = [\varepsilon \times B(LST) + (1 - \varepsilon) \times L_\downarrow] \times \tau + L_\uparrow \quad \text{Eq. 10}$$

in which: L_λ is the thermal infrared radiance; ε is the surface emissivity; *B(LST)* is the thermal radiance of the black body derived from Planck's law at this *LST*; τ is the atmospheric transmittance; and $L_\downarrow$ and $L_\uparrow$ are the atmospheric downward and upward radiations, respectively. Among them, the atmospheric profile information τ, $L_\downarrow$, and

$L_\uparrow$ can be queried on the NASA website (http://atmcorr.gsfc.nasa.gov) by entering the imaging time, center latitude and longitude, and other corresponding parameters.

The derivation shows that the radiance *B(LST)* of a blackbody with a temperature of *LST* (Ermida et al., 2020) in the thermal infrared band is:

$$B(LST) = \frac{[L_\lambda - L_\uparrow - \tau \times (1 - \varepsilon) \times L_\downarrow]}{\varepsilon} \quad \text{Eq. 11}$$

The *LST* was obtained according to the inverse function of Planck's formula, and was calculated as follows:

$$LST = \frac{K_2}{\ln\left(\frac{K_1}{B(LST)} + 1\right)} \quad \text{Eq. 12}$$

in which: K_1 and K_2 are radiation constants. Table 2 summarizes the values of the radiation constants K_1 and K_2 in the Landsat 5/7/8 thermal infrared band.

DEM correction for *LST*

The optical image itself does not have the concept of altitude, but there is a heat exchange effect between the underlying surface and the atmosphere, so *LST* will be affected by altitude. Studies have shown that when the terrain has vertical fluctuations, altitude is negatively correlated with air temperature and ground temperature (Liu and Li, 2005). The *LST* was corrected to eliminate overestimation as follows:

$$LST' = LST - H \times i \quad \text{Eq. 13}$$

in which: *LST'* is the corrected surface temperature (K), *H* is the altitude (m), and *i* is the correction coefficient, which is 0.0064 K km^{-1} (Bailey and Bailey, 2009).

TVDI

The water stress value obtained from the *TVDI* through the feature space can be used to estimate *SM*. Sandholt et al. (2002) conducted a lot of *SM* analysis and found a series of *SM* contours in the characteristic space of *LST* and *NDVI*, that is, the slope of *LST* and *NDVI* under different moisture conditions. Based on this, the *TVDI* was proposed. This was calculated as follows:

$$TVDI = \frac{LST' - LST'_{min}}{LST'_{max} - LST'_{min}} \quad \text{Eq. 14}$$

$$LST'_{min} = a_1 + b_1 \times VI \quad \text{Eq. 15}$$

$$LST'_{max} = a_2 + b_2 \times VI \quad \text{Eq. 16}$$

in which: *LST'* is the surface temperature of any pixel; LST'_{min} and LST'_{max} are the lowest (wet edge equation) and highest (dry edge equation) surface temperatures corresponding to *VI*, respectively; a_1 and a_2 are the coefficients of the dry edge equations; and b_1 and

Table 2. Values of constants K_1 and K_2 of Landsat 5/7/8 *TIR* bands

Radiation constants	Landsat 5 TM Band 6	Landsat 7 ETM+ Band 6	Landsat 8 TIRS Band 10
$K_1/(W \cdot m^{-2} \cdot sr^{-1} \cdot \mu m^{-1})$	607.76	666.09	774.89
K_2/ K	1260.56	1282.71	1321.08

Note: The parameters in the table were obtained from the literature (Jafari and Hasheminasab, 2017).

b_2 are the coefficients of the wet edge equations. In addition to the *NDVI*, this study also used the *SAVI* and *aSAVI* to establish feature spaces of *LST-SAVI* and *LST-aSAVI*, respectively, and fit the feature space and dry-wet edge equations.

Verification of inversion accuracy

The measured *SM* and image data for 2020 and 2021 were used for modeling and verification. We randomly separated 77 % (100 points) of the *SM* dataset as the modeling set, and the remaining 23 % (30 points) was used as the validation set. Different soil layers (0.00-0.10, 0.10-0.20, and 0.20-0.30 m) were modeled and verified. Model construction evaluation used the model simulation value and the real value determination coefficient R^2; accuracy verification used the verification set and the simulation value determination coefficient R^2 and root mean squared error (*RMSE*).

Trend line analysis

Linear propensity estimation is a method of estimating the trends of evaluation parameters in a time series, changes in spatial distribution patterns, and transitions or sudden changes with time by the least squares method. This method can effectively simulate the changing trend of each pixel, thereby reflecting the spatial change characteristics of *SM* in different time periods (Han et al., 2019). The formula is:

$$\theta_{slope} = \frac{n \times \sum_{i=1}^{n} i \times SM_i - \sum_i^n i \sum_i^n SM_i}{n \times \sum_i^n i^2 - (\sum_i^n i)^2} \qquad \text{Eq. 17}$$

in which: θ_{slope} is the slope of the trend line; *n* is the cumulative number of years of monitoring; and SM_i is the *SM* in the *i*-th year. When θ_{slope} >0, the variation trend of *SM* increases, that is, the *SM* content tends to increase; θ_{slope} = 0 means that *SM* content remained stable, while θ_{slope} <0 indicates that *SM* content decreased.

RESULTS

Model

LST–VI feature space

The linear fitting results of the least squares regression of the four *VIs* and *LST* in 2020 and 2021 are shown in figure 3. According to the theory of *TVDI*, the corresponding surface temperature on the dry edge decreases with an increase in the *VI*, and the corresponding surface temperature on the wet edge increases with an increase in the *VI*. Thus, the dry and wet edges or their extension lines intersect to form an angular shape (*LST–VI* feature space). That is, in the feature space, the dry edge and the wet edge show negative and positive correlations with *VI* and *LST*, respectively. Find out the feature space of *VIs* to form a trapezoid or triangle to meet the *TVDI* construction based on the slope of the dry-wet edge equation. The wet edges of the feature spaces of *SAVI-LST* and *aSAVI-LST* showed a weak positive correlation, and the shape of the feature space was trapezoidal. However, the *MSAVI-LST* feature spaces (Figure 3c) showed the same negative correlation as that on the dry edge and the slopes of the dry and wet edges were almost the same. This indicates that extension lines representing the dry and wet edges of the feature space cannot form an angular shape. At the same time, in the *NDVI-LST* feature space, the absolute value of the slope of the dry edge was much larger than that of the wet edge, which means that the dry edge dropped faster than the wet edge, and it could intersect on the extension line to form an angular shape.

In summary, to obtain a credible *TVDI* value, the *MSAVI* needs to be eliminated, the dry and wet edges of *NDVI, SAVI*, and *aSAVI* were all approximately linear, and ranges of R^2 were between 0.73-0.89 and 0.20-0.55, respectively, with a good fitting effect.

The fitting effect of the wet edge was worse than that of the dry edge. The reason may be that the vegetation in the study area belongs to the xerophyte types, such as desert and semi-desert. This type of vegetation has a special organization adapted to desert and arid habitats, which inhibits the loss of water, resulting in a slightly poorer linear fitting effect on wet edges. Therefore, these three *VI-LST* feature spaces were used for *TVDI* calculations to reflect the relationship between vegetation and ground surface temperature.

SM-TVDI Model and Validation

Figure 4 showes the *NDVI, SAVI,* and *aSAVI* combined with *SM* (0.00-0.10 and 0.10-0.20 m) fitting relationship. Based on the p<0.05 significance level test, all showed a good fitting result (R^2 was from 0.53-0.70 and 0.20-0.36; *RMSE* was from 1.30-2.98 %). However, the fitting result of *SM* and *TVDI* at 0.20-0.30 m was R^2 ≤0.15 and *RMSE* >2.95 %, which obviously cannot meet the calculation of *TVDI* or achieve the same as the trend observed in many research results.

The *VIs* had close relationships with 0.00-0.10 m *SM* (surface layer). However, as the soil layer deepened, the relationship between *SM* and *VIs* gradually became discrete or even had no correlation. Therefore, the inversion model performed the inversion for the 0.00-0.20 m *SM* layer and eliminated the 0.20-0.30 m *SM,* as it was not well-fitted (Figures 4g, 4h and 4i). Only *SM* for 0.00-0.20 m were retrieved. When constructing the *SM* inversion model, the R^2 corresponding to the *aSAVI* increased by 0.04 and 0.01 compared with that for the *SAVI*, indicating that the modification of *SAVI* had a positive effect on *SM* inversion in this study area. The *SM* fitting relationships corresponding to *aSAVI* with a good fitting effect (0.00-0.10 m: R^2 = 0.70, *RMSE* = 1.30 %; 0.10-0.20 m: R^2 = 0.36, *RMSE* = 2.05 %) was selected as the inversion models ($SM_{0.00\text{-}0.10\ m} = -6.11 \times TVDI + 5.96$; $SM_{0.10\text{-}0.20\ m} = -6.47 \times TVDI + 6.91$), and their accuracy was verified.

The 0.00-0.10 and 0.10-0.20 m *SM* inversion models were used to verify the accuracy of the image extraction prediction and verification sets (Figure 5). The 0.00-0.10 m *SM* model was verified (R^2 = 0.71 and *RMSE* = 1.15 %), and the predicted and measured sets were almost evenly distributed on both sides of the ideal state. The selected *SM* model of the 0.00-0.10 m soil layer can accurately reflect the water content of 0.00-0.10 m soil layer in

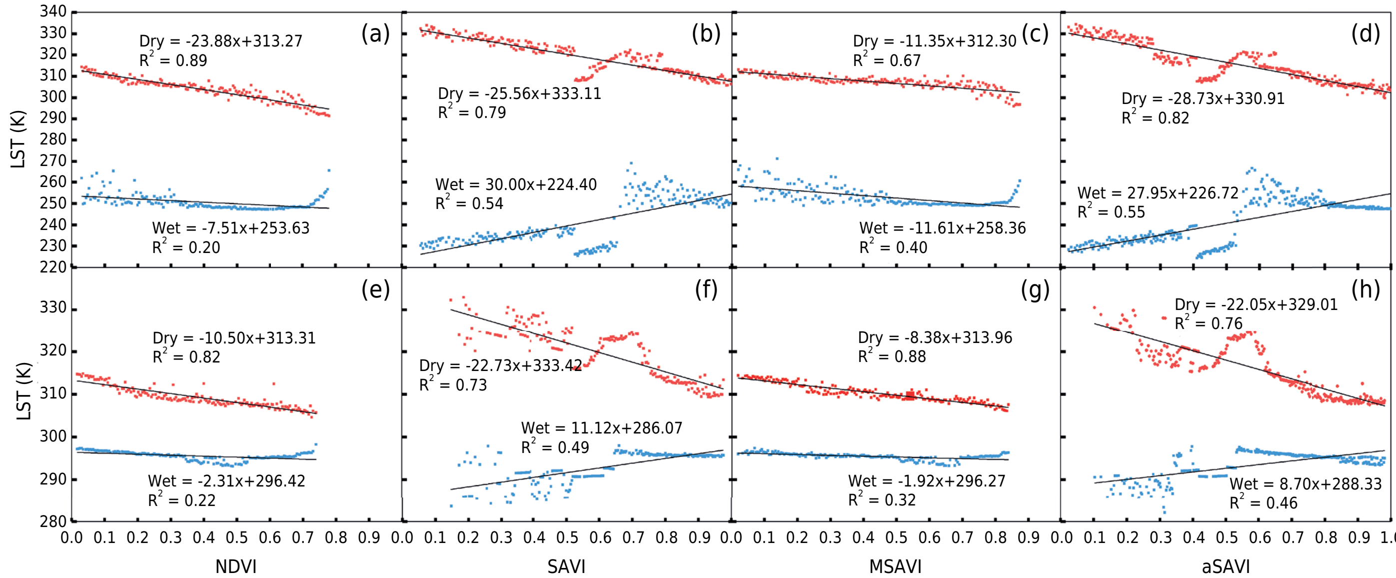

Figure 3. The *LST–VI* feature space. Red and blue sample points fit to form the dry and wet edges. (a) - (d) representative feature space formed by *NDVI, SAVI, MSAVI* and *aSAVI* with *LST* in 2020, respectively. (e) – (h) feature space formed by *NDVI, SAVI, MSAVI*, and *aSAVI* with *VIs-LST* in 2021, respectively.

the study area. The inversion effect of this model for 0.00-0.10 m met the requirements for monitoring moisture variations in the study area. Accuracy of the 0.10-0.20 m model was verified (R^2 = 0.43 and *RMSE* = 1.40 %), and the data were mainly distributed on one side of the prediction set, which was larger than the real data, which led to the deviation of the estimation model. At the same time, the different fitting accuracies of different soil layers verified the difference in the degree of combination of optical remote sensing in inverting surface and deep soil indexes. In summary, the retrieval effect of 0.00-0.10 m *SM* was better than that of 0.10-0.20 m, and both provided a convincing explanation for *SM*.

Application of the SM model

Variation in the mean value of SM from 2000 to 2021

0.00-0.10 m

The mean value of *SM* constantly decreased while fluctuating (Figure 6a), and the fluctuation trend of the three regions was basically synchronous (0.50-3.50 %). During the entire period, the mean *SM* values in the entire study area, irrigated region, and the periphery of irrigated regions were 1.85, 2.47, and 1.36 %, respectively, with the irrigated region much higher than the its periphery (1.82 times).

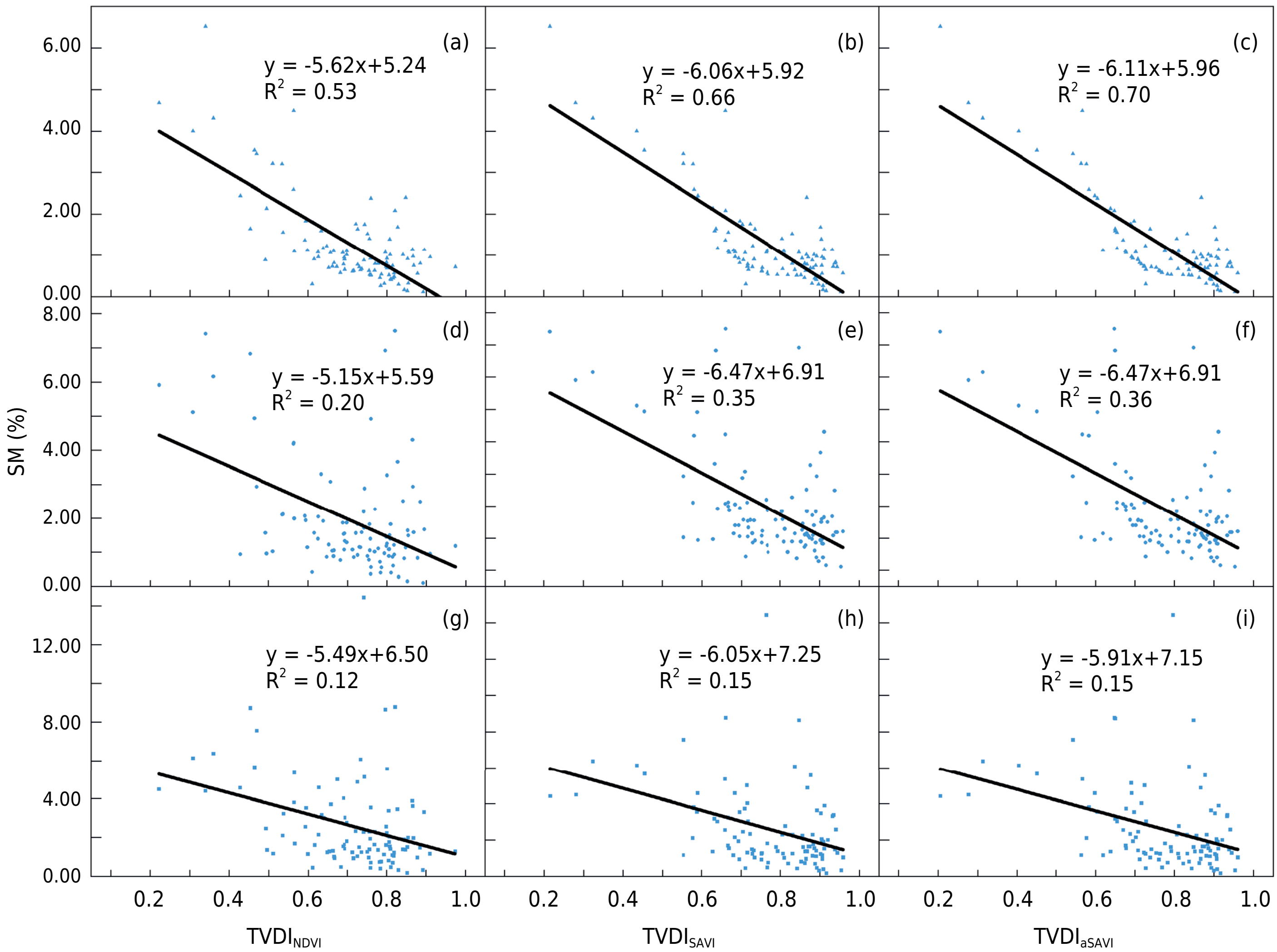

Figure 4. Construction of *SM* and *TVDI* models of various *VIs.* Blue point represent distribution of the measured *SM* and *TVDI* values, and black line represents the fitting results of both variables. The fitting results of *SM* with $TVDI_{NDVI}$, $TVDI_{SAVI}$, and $TVDI_{aSAVI}$ in the 0.00-0.10 m (a–c), the 0.10-0.20 m (d-f), and the 0.20-0.30 m (g-i) soil layers, respectively.

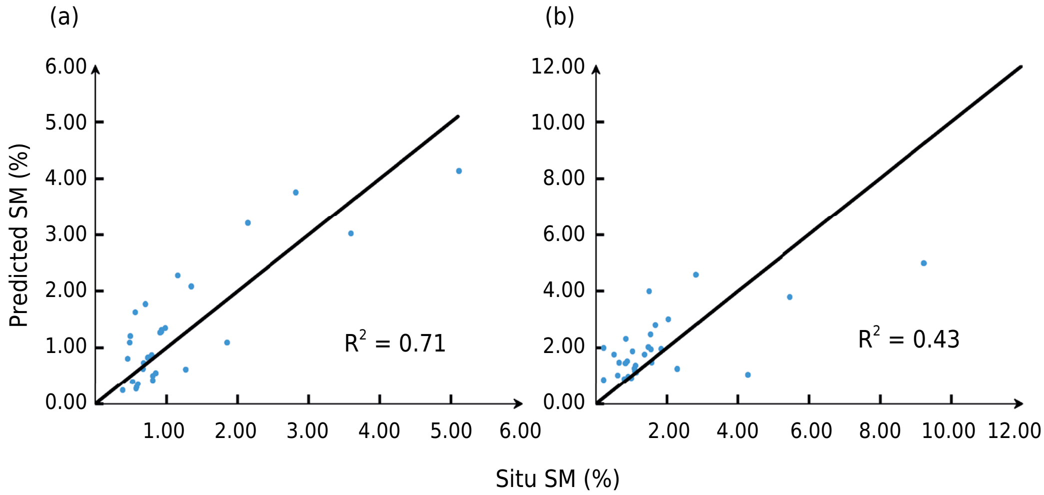

Figure 5. Accuracy verification of prediction models and measured values. Blue points represent the distribution of the *SM* values of verification and prediction sets, and the black line represents the fitting result of the two sets. (a) 0.00-0.10 m, and (b) 0.10-0.20 m.

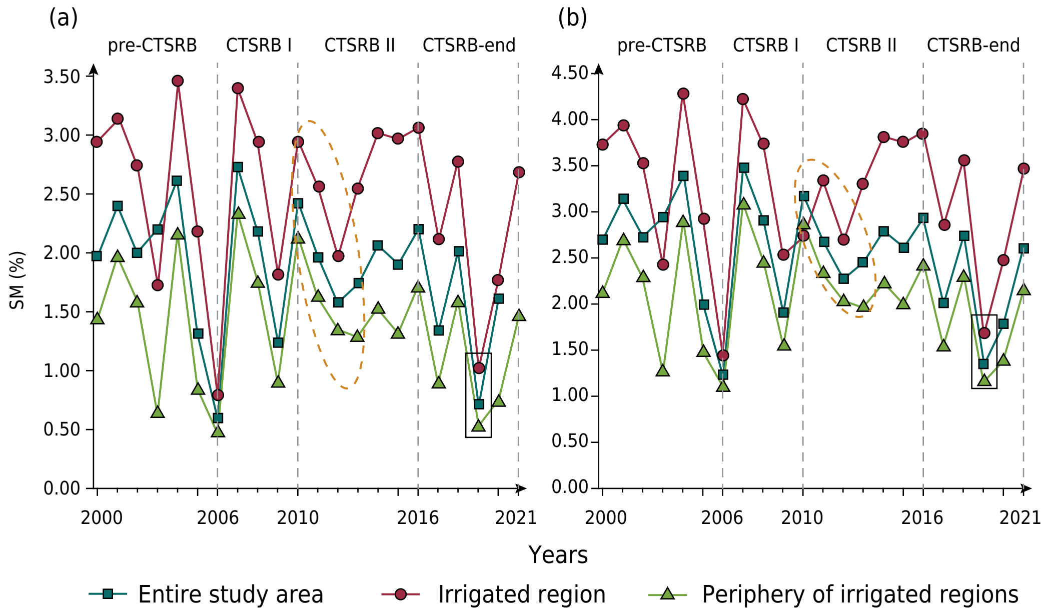

Figure 6. Average variation of *SM* in the study area under time series. Blue, red and green lines represent the average *SM* of entire study area, irrigation area and periphery of the irrigation area over years, respectively; orange virtual coil represents the years in which the *SM* variation was inconsistent across different soil layers, and the gray box indicates the years in which the inversion results were greatly affected by cloud cover. Annual mean change in *SM* in three different regions of 0.00-0.10 m (a), and 0.10-0.20 m (b) soil layers.

In terms of the four periods, only *CTSRB II* showed an increasing trend. During the *pre-CTSRB* period, the mean value of *SM* was in a state of declining volatility (0.60-2.62 %) and reached its lowest value in 2006 (0.60, 0.80, and 0.47 % in the entire study area, irrigated region, and the periphery of irrigated regions, respectively). Then, for *CTSRB I*, the fluctuation state of *SM* was the same as that of *pre-CTSRB* in the first and mid-term (2000-2004). The decline rate of mean *SM* from 2007 to 2009 in the three regions (the entire study area, irrigated region, and the periphery of irrigated regions) was 0.50 %/year, 0.52 %/year, and 0.48 %/year, respectively. The mean value of *SM* increased in 2009-2010, and all three regions reached extremely high levels (2.42, 2.95, and 2.12 %, respectively) in 2010. In *CTSRB II*, there was a one-year delay (the orange circle in Figure 6a) in the process of *SM* decreasing in the periphery of irrigated regions compared to the irrigation regions (4 years), and the rate of decrease was 64.71 % of that of the irrigated regions.

From 2013 to 2016, all three regions showed different degrees of increase. Soil moisture in the periphery of irrigated regions (0.43 %) increased steadily, and the irrigated region changed sharply (1.10 %). After this time, the *SM* of the three regions showed more consistent changes. Likewise, the mean value of *SM* during *CTSRB-end* also declined, but the decline was not too large. The ranges of variation in the entire study area, irrigated region, and the periphery of irrigated regions were 1.33-2.01, 1.77-2.68 and, 0.74-1.58 %, respectively.

0.10-0.20 m

Overall, the annual average *SM* of 0.10-0.20 m was larger than that of 0.00-0.10 m, but the variation trend of the two soil layers was relatively consistent (Figure 6b*)*. The *SM* in the irrigated region was 1.6 times that of the periphery of irrigated regions, but in 2009, with the implementation of restoration measures, the peak value of the irrigated region and the valley bottom in the periphery of irrigated regions were both delayed, which was different from 0.00-0.10 m. Specifically, the entire study area and periphery of irrigated regions peaked in 2010 (3.17, 2.85 %) but the irrigated region was delayed until 2011 (3.33 %). The periphery of the irrigated regions reached the bottom of the valley in the same pattern as 0.00-0.10 m, that is, compared to the entire study area and the irrigated region reaching the bottom of the valley in 2012, the periphery of irrigated regions showed a lag and bottomed out in 2013.

Spatial variation in the trend of SM in different periods

0.00-0.10 m

The spatial distribution of the slope line (θ_{slope}) of *SM* in different periods is shown in figures 7a, 7b, 7c, 7d and 7e. During *pre-CTSRB* (Figure 7a), more than 90 % of the three study regions showed a decreasing trend and only a few places showed an increasing trend. The boundary between the irrigated region and the periphery of irrigated regions was not obvious and showed a sharp decreasing trend (<-0.2). In *CTSRB I* (Figure 7b), *SM* increased sharply compared to the previous period; however, this varied spatially: first, most of the irrigated region continued to show a significant downward trend, and only a small area in the south of the central part had a significant increasing trend. Second, in the middle and northeastern part of the periphery of the irrigation region, there was a strip-like increase trend of *SM* (0.01-0.20), and all the others except the southeast part changed from a significant decreasing trend to a decreasing trend. Finally, the central and northeast *SM* of the whole region showed an increasing trend, while the southwest showed little change compared with *pre-CTSRB*. During *CTSRB II*, due to the implementation of ecological water conveyance measures, *SM* showed a significant increasing trend in the entire region, especially in the irrigation region.

However, this trend varied spatially: first, the variation trend of *SM* in the irrigated region showed a significant increasing trend (>0.20), which was 0.40 higher than that in *CTSRB I*. Second, there was a hysteresis phenomenon in the *SM* variation in the periphery of the irrigation region; however, it basically showed an increasing trend, except in the southwest. Finally, in the entire region, the variation was more obvious in the central part than in the other parts. The variation trend of *SM* during *CTSRB-end* was related to the lagged phenomenon of water migration, which showed a decreasing trend from southwest to northeast in the whole region, but the range of the increasing trend was obviously reduced. The basic variation trend of *SM* in the irrigation region was increased (southeast and central) directly to a significant decrease (northwest), while the periphery of the irrigation region shows a steadily decreasing trend. The

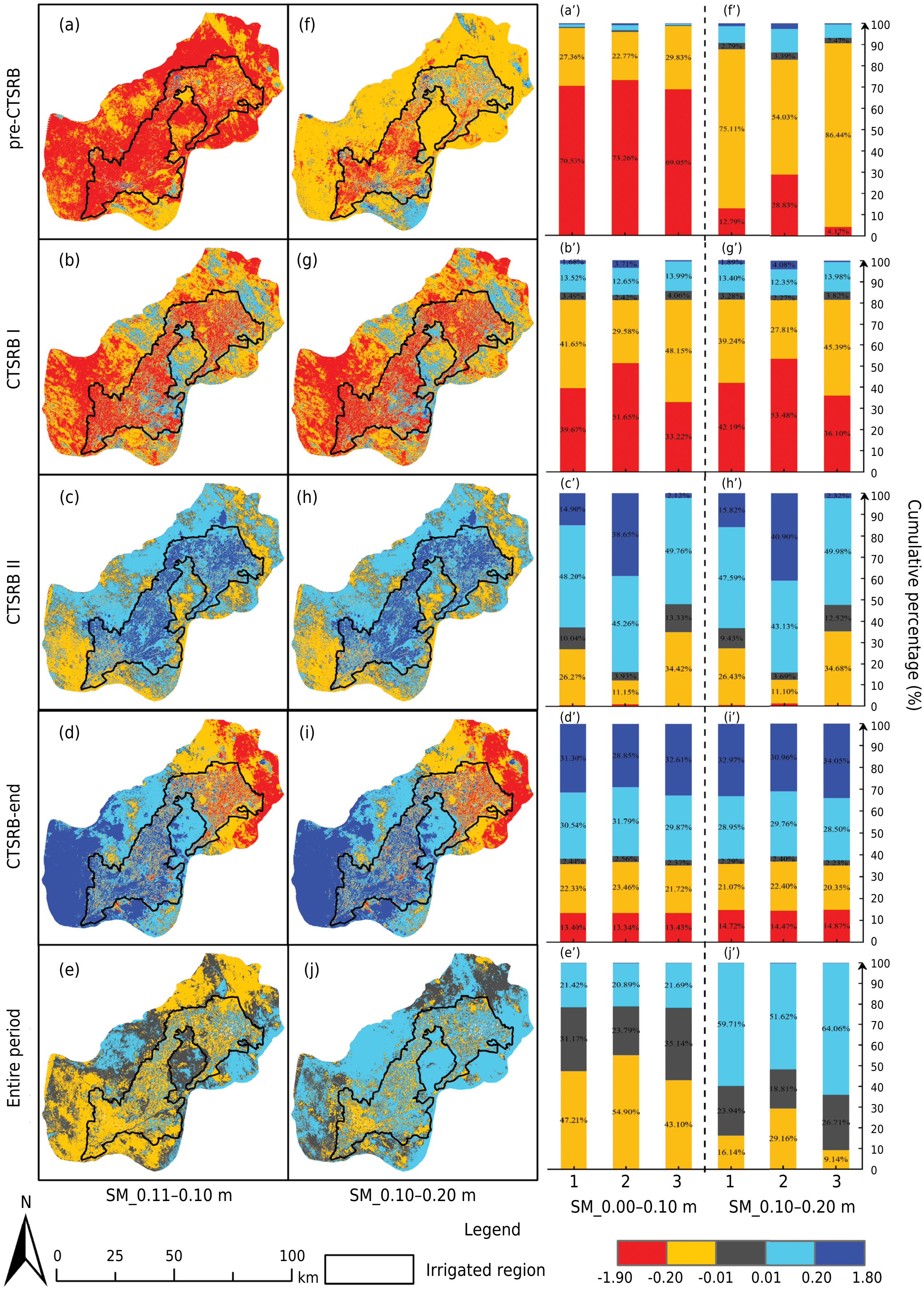

Figure 7. Spatial distribution of θ_{slope} and cumulative percentage of area for *SM* in different soil layers and periods. Red, orange, gray, blue and dark blue indicate that *SM* obviously decreased, decreased, remains constant, increased and obviously increased in different periods, respectively. I, II and III represent the entire region, irrigation region and periphery of irrigation region, respectively. (a) - (e) and (f) – (j) denote the *SM* change trend image during the *pre-CTSRB, CTSRB-I, CTSRB-II, CTSRB-end* and entire period in 0.00-0.10 m and 0.10-0.20 m soil layers, respectively. (a') – (e') and (f') – (j') show the corresponding pixel proportion maps, respectively.

changing trend in the periphery of the irrigation area is less than the complexity of the irrigation area, and the boundary between the two areas is very clear.

Soil moisture showed a slight decline throughout the studied period. First, the irrigation region had a downward trend as a whole (-0.20–0.01) but an increasing trend in parts of the central and northeastern regions. Second, the southwest and northeast parts of the irrigated region showed a decreasing trend, but in the middle part of the irrigated region, *SM* did not change (-0.01–0.01) in addition to the increasing trend. Finally, there was a decreasing-increasing-decreasing trend in the entire region from northeast to southwest, and the distribution of regions where *SM* did chang was uneven.

0.10-0.20 m

During the *pre-CTSRB* period of *SM* (Figures 7f, 7g, 7h, 7i and 7j), the decrease in *SM* in different regions was slightly lower than that of topsoil. First, the northeastern part of the irrigation region showed an increasing trend, and the decrease at the other layers was slower than in 0.00-0.10 m. Second, the overall periphery of the irrigation region decreased sharply compared with the topsoil and became a steadily decreasing trend. Moreover, *SM* in the northwest of the irrigation region and southeast of the periphery of the irrigation region had increasing trends. The *CTSRB I, CTSRB II,* and *CTSRB-end* periods had the same changing trends as the corresponding periods of the surface soil, but with different changing trend distributions. Specifically, the trend is caused by an insignificant gap in the distribution of the trend variation, and the distribution of *CTSRB I* and *CTSRB-end* of 0.10-0.20 m sharply increased compared with that of *SM* in the topsoil layer, while the distribution of both changed and unchanged soil layers decreased. *CTSRB II* showed a significant decrease-decrease-increase trend, while the other periods showed a decrease. From the entire period, the *SM* of 0.10-0.20 m showed an increasing trend and the part corresponding to the decrease of 0.00-0.10 m showed an increasing or unchanged trend.

Relationship between mean θ_{slope} and the percentage of area where *SM* fell in different periods

0.00-0.10 m

The area and content of *SM* change in the three regions (the entire region, irrigated region, and periphery of the irrigated region) during *pre-CTSRB* were all reduced, and the area reduced by *SM* was more than 96 % (Figure 8a). The periphery of the irrigated region had the largest reduction in area (99.10 %), and the irrigated region had the largest reduction in *SM* content (θ_{slope} = 0.28).

The *CTSRB I* period showed the same trend as the previous period, but the area and content decreased compared with the previous stage. The three regions showed an increasing trend in the *CTSRB II* stage and the increased area (85.64 %) and *SM* content (0.17) of the irrigation region were the highest. *CTSRB-end* continued the trends of *CTSRB-II*. There was no significant difference between the *SM* content and decreased area of the three regions. Finally, in the entire period, the content of *SM* (-0.02, -0.01, -0.01) almost did not change, but the distribution area of *SM* reduction showed a decreasing trend: irrigation region > entire region > non-irrigation region. It was also found that the content of *SM* was obvious negatively correlated with the decreasing area (R^2 = 0.92); that is, as the distribution area of *SM* decreased, its content increased. Based on these results, *SM* tended to increase during the total period.

0.10-0.20 m

At 0.10-0.20 m (Figure 8b), the trends of *SM* content and area change in the four periods were basically the same. However, R^2 decreased from 0.92 to 0.74, and the accuracy of the performance also decreased in *CTSRB I, CTSRB II,* and *CTSRB-end*. During *pre-CTSRB,*

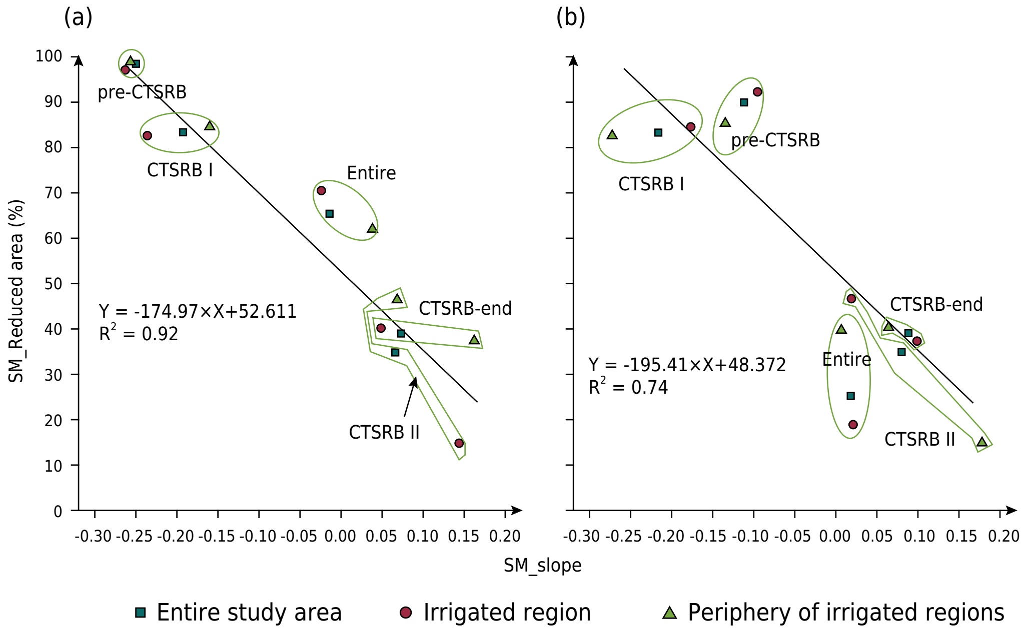

Figure 8. Trend line slope of *SM.* Blue, red and green points represent the entire study area, irrigation area and periphery of irrigation area, respectively. Each closed green figure represents the *SM* change trend and area distribution of the same soil layer in the same period, and black line represents the fitting results of these two variables. (a) 0.00-0.10 m, (b) 0.10-0.20 m.

the distribution areas of the *SM* reduction in 0.10-0.20 m in the entire study area, irrigated regions, and periphery of the irrigated regions were reduced by 89.77, 85.21 and, 92.02 %, respectively, compared with the 0.00-0.10 m, and the *SM* content was also reduced. The variation in *SM* in *CTSRB I* was larger than that in 0.00-0.10 m. There was no significant difference between *CTSRB II* and *CTSRB-end* of 0.00-0.10 m. In the whole time series, the *SM* content of 0.10-0.20 m did not change sharply, and the distribution area of *SM* reduction showed an opposite trend to that of 0.00-0.10 m, with the periphery of the irrigated area increasing the most (81.50 %). Similarly, there was a negative correlation (0.74) between the reduced distribution content and the content of 0.10-0.20 m *SM*, but the trend of 0.10-0.20 m layer was opposite to that of 0.00-0.10 m layer, and it tended to decrease.

DISCUSSION

Water migration in different periods

Soil moisture is an important driving force of the ecosystem, and its migration law is an important factor that provides a scientific basis for ecological water demand, ecological restoration, and water resources management (Yang and Fu, 2017). With the implementation of the ecological water transportation project in *CTSRB II*, significant changes occurred in the spatiotemporal distribution of *SM* in different soil layers and between irrigated regions and the periphery of irrigated regions. There are several reasons for these changes: first, soil types with a large proportion of sand are generally in arid and semi-arid areas, and the proportion of sand decreases as the soil deepens. Second, the water storage capacity of the soil in the irrigated region is higher than that in the periphery of the irrigated region (Mesbah and Kowsar, 2011). Finally, the vegetation grown in these two regions differed greatly in the degree or ability of *SM* utilization. Precipitation and evapotranspiration are key factors affecting the life cycle of vegetation in the periphery of irrigated regions, especially in arid and semi-arid areas (Li et al., 2014).

Therefore, the micro-environment differences between irrigated regions and their peripheries may lead to differing or even opposite water migration results. Indeed, in this study, the direction of ecological water transport during *CTSRB-end* was opposite to that of *SM*. This indicates that the amount of water transported to the region was not enough to replenish the lost water (especially in the northeast portion of the study area). The main possible reasons are water infiltration fast and soil water supersaturation (Cox et al., 2018) and surface evaporation and loss caused by the climate (Lang et al., 1974). From the perspective of evapotranspiration, the northeast regions were much larger than the southwest after the movement of water; from the water saturation point of view, when the northeast regions reached saturation, the southwest maybe the time when *SM* increased sharply; from the perspective of water infiltration, the difference in *DEM* were caused *SM* gathers and disperses in a local region.

Relationship between *SM* and *VC*

From the relationship between *VC* and *SM* (Figure 9), we can see that the *SM* change trends of 0.00-0.10 and 0.10-0.20 m were relatively consistent. In *pre-CTSRB*, irrigation consumed a lot of groundwater, and *SM* (rising) can theoretically meet the growth of vegetation; however, *VC* (declining) does not match it. That is, adequate water supply but poor vegetation growth (Zhou et al., 2013).

In *CTSRB I*, *SM* fluctuated greatly, but *VC* showed a single peak shape and reached its peak in 2008. The *CTSRB* was launched in 2006 to curb the trend of destruction by planting grass and shrubs with strong stress resistance. In the initial stage of introducing new vegetation, there was a greater demand for *SM*, but as the environment tempers it, a part of the vegetation species was naturally selected to remain. Through the continuous repetition of this process, the environmental carrying capacity of the study area was enhanced, so the *SM* fluctuated and the *VC* showed different stages of rapid growth and decline to stability.

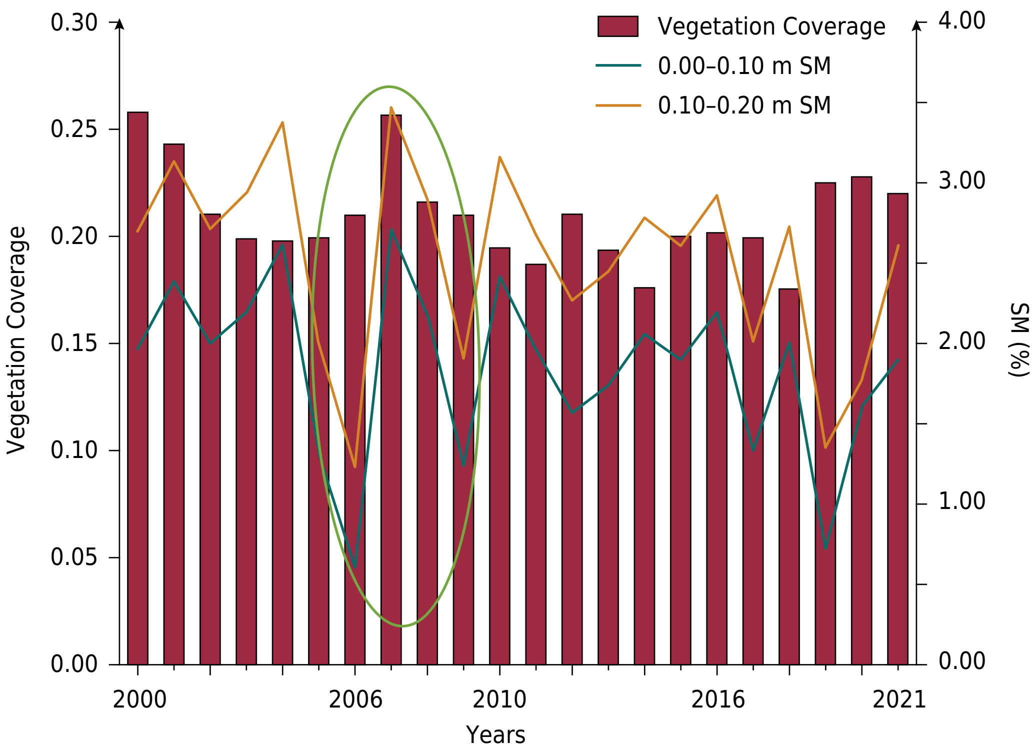

Figure 9. Relationship between *VC* and *SM*. Red columns indicates *VC* over time; blue and orange lines represent the mean *SM* of the study area in the 0.00-0.10 and 0.10-0.20 m soil layers, respectively. Green circle indicates the year that *SM* and *VC* had the same trend.

The *SM* and *VC* in *CTSRB II* showed a competitive relationship (wane and wax) during 2011-2014, and the two showed the same upward trend from 2015 to 2016. This stage is a continuation of the previous period and plays the role of evaluation and remedy in terms of the degree of recovery. This stage can be summarized as the process of vegetation domestication from 2011 to 2014, and the vegetation adapted to the study area from 2015 to 2016; *SM* also has a trend of picking up.

During *CTSRB-end*, the *SM* (decrease) and vegetation showed opposite changes. Specifically, vegetation was only affected by the decline in *SM* in 2018 and remained at a high level (>0.22) in the subsequent period. In summary, the fluctuation range of the *VC* was weaker than that of the *SM*. On the one hand, it shows that the introduced vegetation adapted to the environment of the study area and contributed to ecological improvement (Thieltges et al., 2006). On the other hand, the regulatory feedback of vegetation and water promoted soil restoration to a certain extent (Li et al., 2018). Similarly, the weakness and particularity of the soil will affect this feedback (Yang et al., 2014). Therefore, the insignificant change in vegetation and the deterioration of the ecological environment indicate that the interaction mechanism of these two can contain degradation or positively affect secondary succession (Zhao et al., 2018).

Ecological effects evaluation of the *CTSRB* from the perspective of *SM*

Unconventional changes in *SM* are major factors that cause soil disturbance and erosion, and climatic factors (precipitation, temperature, and groundwater level) often lead to relative changes in *SM*, thereby affecting the carrying capacity of soil (Allman et al., 2017). A lack of *SM* will eventually lead to a decline in the quality of soil and vegetation (Guo, 2021a). Therefore, the soil-carrying capacity can reflect the relationship between organisms and the environment.

In arid and semi-arid regions, it is difficult for vegetation on the periphery of irrigated areas to obtain groundwater; therefore, *SM* is mainly derived from precipitation (Guo, 2021b). Due to limited precipitation, the balance between vegetation and *SM* determines the area’s ecological environment. The threshold of the soil’s ability to carry water in the periphery of irrigated areas determines the quality of the environment.

The regulation of the relationship between water and vegetation is not limited to *SM* but also impacts soil quality; that is, the environmental carrying capacity of soil. In Luvisol, Stagnic Luvisol, Gleysols, and Cambisols, *SM* and other factors affect the soil carbon emission capacity, which subsequently affects the organic carbon content in cultivated areas (Wang et al., 2015). In northern Finland (60 - 70 °N), changes in *SM*, frost, and snow in the winter can change the soil carrying capacity, especially in bare regions without tree cover (Kellomaki et al., 2010). The relationship between *SM* and groundwater can reflect the carrying capacity to a certain extent (Besser et al., 2017). The depletion of local groundwater and the carrying capacity of soil has been greatly restricted, leading to soil degradation. To further increase revenue, farmers were no longer satisfied with the current harvest, and reclaiming farmland at will, so gradually formed a vicious cycle, which was “development of agriculture-consumption of soil carrying capacity-blind irrigation-soil degradation” (Aarnoudse et al., 2012; Han et al., 2019). The improvement of vegetation in different areas can promote ecological restoration to contain degradation (Hedl et al., 2017). Whether vegetation improvement can achieve a good ecological restoration effect depends on selecting appropriate vegetation populations and retaining vegetation after natural selection.

In summary, the soil carrying capacity in irrigated areas in this study area decreased due to agricultural development. It is difficult for vegetation in non-irrigated areas to actively access groundwater, thus relying on precipitation to maintain the balance between vegetation and *SM*. Moreover, precipitation in the study area (arid and semi-arid) is limited, and there is a gap between soil water supply and demand (Ren et al., 2014).

The soil in the periphery of the irrigated areas was limited by an insufficient supply of *SM*, which reduced the soil quality, even leading to erosion or degradation. Therefore, to use soil sustainably and efficiently, it must be improved or repaired. Good ecological restoration projects can play a positive role in local development. Indeed, looking at the five years since the end of the *CTSRB*, the capacity to preserve moisture and water storage increased; starting from an insufficient supply of groundwater before 2006, the soil carrying capacity increased throughout the project life. The project also showed its promoting effect through the stabilization of *VC*, demonstrating that the project improved the soil carrying capacity and indicating that the project promoted the ecological restoration of the entire region.

In addition, different scholars evaluated the ecological restoration effect of *CTSRB* from the perspectives of groundwater level (Hao et al., 2017), vegetation coverage (Youhao et al., 2007), desertification (Sun et al., 2006), and vegetation diversity (Wu et al., 2021), and proved that *CTSRB* played a positive role in the restoration of the Minqin ecological environment. This study took a different approach and interpreted the ecological restoration effect of the *CTSRB* from the perspective of *SM*. This approach constitutes not only an effective attempt to evaluate the effect of *CTSRB* ecological restoration but also provides evidence for the evaluation of the effect of ecological restoration projects in arid regions around the world.

Relationship between *SM* changes, groundwater level and vegetation restoration

Before 2006, the study area supported agricultural development, utilizing a large amount water resources, especially groundwater resources. This emphasis on economy rather than ecology resulted in a sharp decline in groundwater levels, obvious vegetation degradation, and increasingly serious eco-environmental problems. In our study, the *SM* of the 0.00-0.20 m soil layer showed a downward trend during *pre-CTSRB*, and the *SM* decline was greater in the 0.00-0.10 m layer than the 0.10-0.20 m layer. Studies have shown that the groundwater level (Hao et al., 2017) and vegetation (Wu et al., 2021) of the Minqin area during the *CTSRB* period was more recovered than the *pre-CTSRB* period. During *CTSRB*, compared with *pre-CTSRB*, *SM* of 0.00-0.10 m gradually decreased while the soil layer of 0.10-0.20 m gradually increased. We can infer that under the effects of *CTSRB*, ecological environment conditions such as groundwater level and vegetation improved in the Minqin basin, while soil moisture increased (Wu et al., 2010).

Zheng et al. (2021) found that during restoration efforts aiming to revert farmlands to forests and grasslands, the initial growth of vegetation corresponds to the sharp decrease and stable consumption of *soil moisture*. The amount of water needed for growth decreases and the *soil moisture* increases to a certain extent, which is similar to our findings of fluctuating water levels in the study area during the *CTSRB-I* and *II* periods. Rüdiger Bunk et al. (2017) found that the groundwater level in the study area rose in recent years, which can effectively reduce the vertical infiltration rate of water, and further curb the rapid infiltration of *SM*. The retention of this component of *SM* can promote vegetation growth and ecological restoration. Therefore, we believe that *SM* may not directly promote ecological restoration, but increases in *SM* can indirectly reflect improved ecological environments.

CONCLUSIONS

aSAVI was established by adjusting *L* and increasing the *SWIR* band by *SAVI,* and the *LST* was corrected by *DEM*. The improved TVDI model improves the inversion accuracy, and the model can predict the SM of 0.00-0.20m soil layer better ($SM_{0.00\text{-}0.10\ m} = -6.11 \times TVDI + 5.96$; $SM_{0.10\text{-}0.20\ m} = -6.47 \times TVDI + 6.91$). However, *MSAVI* was not sensitive to the performance of the study area.

The mean value of *SM* (soil moisture) constantly decreased while fluctuating, and the fluctuation trends of the entire study area, irrigated region, and periphery of irrigated regions were all basically synchronous. Soil moisture decreased in most areas during *pre-CTSRB* (0.00-0.10 m: 97.72 %, 0.10-0.20 m: 87.74 %) → increased in individual areas during *CTSRB I* (0.00-0.10 m: 15.19 %, 0.10-0.20 m: 15.39 %) → increased in most areas in *CTSRB II* (0.00-0.10 m: 63.08 %, 0.10-0.20 m: 63.4 %) → the increased area shifted from the central and eastern part of the previous period to the central and western part during *CTSRB-end* (0.00-0.10 m: 61.84 %, 0.10-0.20 m: 61.94 %). The change trend in the 0.10-0.20 m soil layer was larger than that in 0.00-0.10 m layer. The areas of increased *SM* in the past 22 years were 21.35 % at 0.00-0.10 m and 59.66 % at 0.10-0.20 m. There was a negative correlation between the mean θ_{slope} of *SM,* and the percentage of area where *SM* had fallen in different periods.

With the *CTSRB* implementation, the decline rate of *SM* in the study area gradually slowed down, while the area where *SM* content increased gradually expanded. Therefore, from the perspective of *SM*, *CTSRB* influenced ecological restoration in Minqin Basin.

Although we only provided the evaluation of a short period after the completion of the project, the shortcoming is that it is easy to generalize, but we also quantified the evaluation of ecological restoration with single data or auxiliary data. The next step is to conduct a continuous follow-up evaluation or add modeling and mechanism studies such as *SM* and salt vegetation interaction.

ACKNOWLEDGMENTS

The authors would like to express their sincere appreciation and gratitude to the National Natural Science Foundation of China (Grant No.41907406 and 32160338) and the Science and Technology Innovation Fund of Gansu Agricultural University (GAU-KYQD-2018-23) for their financial support, as well as the editors and reviewers for their constructive comments and suggestions.

AUTHOR CONTRIBUTIONS

Conceptualization: Yuanyuan Hao (equal) and Xin Liu (equal).

Formal analysis: Xin Liu (lead).

Funding acquisition: Yuanyuan Hao (lead).

Investigation: Xin Yang (equal) and Ziyan Zhou (equal).

Methodology: Xin Liu (lead).

Resources: Ruifang Zhang (equal) and Tao Yu (equal).

Software: Xin Liu (lead).

Supervision: Limin Hua (equal) and Wenxia Cao (equal).

Validation: Yuanyuan Hao (lead).

Visualization: Ruifang Zhang (equal) and Ziyan Zhou (equal).

Writing – original draft: Xin Liu (lead).

Writing – review & editing: Yuanyuan Hao (equal) and Xin Liu (equal).

REFERENCES

Aarnoudse E, Bluemling B, Wester P, Qu W. The role of collective groundwater institutions in the implementation of direct groundwater regulation measures in Minqin County, China. Hydrogeol J. 2012;20:1213-21. https://doi.org/10.1007/s10040-012-0873-z

Allman M, Jankovsky M, Messingerova V, Allmanova Z. Soil moisture content as a predictor of soil disturbance caused by wheeled forest harvesting machines on soils of the Western Carpathians. J For Res. 2017;28:283-9. https://doi.org/10.1007/s11676-016-0326-y

Assi AT, Mohtar RH, Braudeau E. Soil pedostructure-based method for calculating the soil-water holding properties. MethodsX. 2018;5:950-8. https://doi.org/10.1016/j.mex.2018.08.006

Bailey RG, Bailey RG. Ecosystem geography: From ecoregions to Sites. 2nd ed. New York: Springer; 2009.

Besser H, Mokadem N, Redhouania B, Rhimi N, Khlifi F, Ayadi Y, Omar Z, Bouajila A, Hamed Y. GIS-based evaluation of groundwater quality and estimation of soil salinization and land degradation risks in an arid Mediterranean site (SW Tunisia). Arab J Geosci. 2017;10:350-70. https://doi.org/10.1007/s12517-017-3148-0

Bunk R, Behrendt T, Yi ZG, Andreae MO, Kesselmeier J. Exchange of carbonyl sulfide (OCS) between soils and atmosphere under various CO_2 concentrations. J Geophys Res-Biogeosci. 2017;122:1343-58. https://doi.org/10.1002/2016jg003678

Carlson TN, Dodd JK, Benjamin SG, Cooper JN. Satellite estimation of the surface-energy balance, moisture availability and thermal inertia. J Appl Meteorol. 1981;20:67-87. https://doi.org/10.1175/1520-0450(1981)020<0067:Seotse>2.0.Co;2

Carlson TN, Perry EM, Schmugge TJ. Remote estimation of soil-moisture availability and fractional vegetation cover for agricultural fields. Agric For Meteorol. 1990;52:45-69. https://doi.org/10.1016/0168-1923(90)90100-k

Charlton M. Small scale soil-moisture variability estimated using ground penetrating radar. In: Proceedings of the 8th International Conference on Ground Penetrating Radar (GPR 2000); 2000 May 23-26; Univ Queensland, Gold Coast, Australia. Bellingham: Spie-Int Soc Optical Engineering; 2000. p. 798-804.

Chatterjee RS, Singh N, Thapa S, Sharma D, Kumar D. Retrieval of land surface temperature (LST) from landsat TM6 and TIRS data by single channel radiative transfer algorithm using satellite and ground-based inputs. Int J Appl Earth Obs. 2017;58:264-77. https://doi.org/10.1016/j.jag.2017.02.017

Chen JA, Wang CZ, Jiang H, Mao LX, Yu ZR. Estimating soil moisture using Temperature-Vegetation Dryness Index (TVDI) in the Huang-huai-hai (HHH) plain. Int J Remote Sens-Basel. 2011;32:1165-77. https://doi.org/10.1080/01431160903527421

Chen XH, Guo ZF, Chen J, Yang W, Yao YM, Zhang CS, Cui XH, Cao X. Replacing the red band with the red-SWIR band ($0.74\rho_{red}+0.26\rho_{swir}$) can reduce the sensitivity of vegetation indices to soil background. Remote Sens-Basel. 2019;11:851-66. https://doi.org/10.3390/rs11070851

Cosh MH, Jackso TJ, Smith C, Toth B, Berg AA. Validating the BERMS in situ soil water content data record with a large scale temporary network. Vadose Zone J. 2013;12:1-5. https://doi.org/10.2136/vzj2012.0151

Cox C, Jin LX, Ganjegunte G, Borrok D, Lougheed V, Ma L. Soil quality changes due to flood irrigation in agricultural fields along the Rio Grande in western Texas. Appl Geochem. 2018;90:87-100. https://doi.org/10.1016/j.apgeochem.2017.12.019

Ermida SL, Soares P, Mantas V, Gottsche FM, Trigo IE. Google earth engine open-source code for land surface temperature estimation from the landsat series. Remote Sens-Basel. 2020;12:1471-92. https://doi.org/10.3390/rs12091471

Feng HX, Qin QM, Li BY, Liu F, Jiang HB, Dong H, Wang JL, Liu MC, Zhang N. The new method monitoring agricultural drought based on SWIR-Red spectrum feature space. Spectrosc Spectr Anal. 2011a;31:3069-73. https://doi.org/10.3964/j.issn.1000-0593(2011)11-3069-05

Feng SY, Huo ZL, Kang SZ, Tang ZJ, Wang FX. Groundwater simulation using a numerical model under different water resources management scenarios in an arid region of China. Environ Earth Sci. 2011b;62:961-71. https://doi.org/10.1007/s12665-010-0581-8

Feng SY, Kang SZ, Huo ZL, Chen SJ, Mao XM. Neural networks to simulate regional ground water levels affected by human activities. Ground Water. 2008;46:80-90. https://doi.org/10.1111/j.1745-6584.2007.00366.x

Gillies RR, Carlson TN. Thermal remote-sensing of surface soil-water content with partial vegetation cover for incorporation into climate-models. J Appl Meteorol. 1995;34:745-56. https://doi.org/10.1175/1520-0450(1995)034<0745:Trsoss>2.0.Co;2

Guha S, Govil H, Dey A, Gill N. A case study on the relationship between land surface temperature and land surface indices in Raipur City, India. Geogr Tidsskr. 2020;120:35-50. https://doi.org/10.1080/00167223.2020.1752272

Guo LB, Bao YH, Bao G, Hai QS. Inner Mongolia soil moisture retrieved from MODIS image and TVDI model. In: Proceedings of the Conference on PIAGENG - Image Processing and Photonics for Agricultural Engineering; 2009 Jul 11-12; Zhangjiajie, Peoples R China. Bellingham: Proceedings of SPIE-The International Society for Optical Engineering; 2009. p. 02-10.

Guo ZS. Soil water carrying capacity for vegetation. Land Degrad Dev. 2021a;32:3801-11. https://doi.org/10.1002/ldr.3950

Guo ZS. Soil hydrology process and rational use of soil water in desert regions. Water. 2021b;13:2377. https://doi.org/10.3390/w13172377

Gutman G, Ignatov A. The derivation of the green vegetation fraction from NOAA/AVHRR data for use in numerical weather prediction models. Int J Remote Sens. 1998;19:1533-43. https://doi.org/10.1080/014311698215333

Hamidisepehr A, Sama MP, Turner AP, Wendroth OO. A method for reflectance index wavelength selection from moisture-controlled soil and crop residue samples. T ASABE. 2017;60:1479-87. https://doi.org/10.13031/trans.12172

Han Q, Fan HB, Peng J, Zhou LL, Gan L. Pleiotropic function of vitamin C on fatty acids in liver and muscle of juvenile grass carp (Ctenopharyngodon idella). Aquaculture. 2019;512:734352. https://doi.org/10.1016/j.aquaculture.2019.734352

Hao YY, Xie YW, Ma JH, Zhang WP. The critical role of local policy effects in arid watershed groundwater resources sustainability: A case study in the Minqin oasis, China. Sci Total Environ. 2017;601-602:1084-96. https://doi.org/10.1016/j.scitotenv.2017.04.177

Hedl R, Sipos J, Chudomelova M, Utinek D. Dynamics of herbaceous vegetation during four years of experimental coppice introduction. Folia Geobot. 2017;52:83-99. https://doi.org/10.1007/s12224-016-9281-9

Holzman ME, Rivas R, Piccolo MC. Estimating soil moisture and the relationship with crop yield using surface temperature and vegetation index. Int J Appl Earth Obs. 2014;28:181-92. https://doi.org/10.1016/j.jag.2013.12.006

Holzman ME, Rivas RE, Bayala MI. Relationship between TIR and NIR-SWIR as indicator of vegetation water availability. Remote Sens-Basel. 2021;13:3371-90. https://doi.org/10.3390/rs13173371

Huete AR. A soil-adjusted vegetation index (SAVI). Remote Sens Environ. 1988;25:295-309. https://doi.org/10.1016/0034-4257(88)90106-x

Jackson TJ, Bindlish R, Cosh MH, Zhao TJ, Starks PJ, Bosch DD, Seyfried M, Moran MS, Goodrich DC, Kerr YH, Leroux D. Validation of soil moisture and ocean salinity (SMOS) soil moisture over watershed networks in the U.S. IEEE T Geosci Remote. 2012;50:1530-43. https://doi.org/10.1109/tgrs.2011.2168533

Jafari R, Hasheminasab S. Assessing the effects of dam building on land degradation in central Iran with Landsat LST and LULC time series. Environ Monit Assess. 2017;189:74-89. https://doi.org/10.1007/s10661-017-5792-y

Kasim N, Tiyip T, Abliz A, Nurmemet I, Sawut R, Maihemuti B. Mapping and modeling of soil salinity using worldview-2 data and EM38-KM2 in an arid region of the Keriya River, China. Photogramm Eng Rem S. 2018;84:43-52. https://doi.org/10.14358/pers.84.1.43

Kazemzadeh M, Salajegheh A, Malekian A, Liaghat A, Hashemi H. Soil moisture change analysis under watershed management practice using in situ and remote sensing data in a paired watershed. Environ Monit Assess. 2021;193:299. https://doi.org/10.1007/s10661-021-09078-y

Kellomaki S, Maajarvi M, Strandman H, Kilpelainen A, Peltola H. Model computations on the climate change effects on snow cover, soil moisture and soil frost in the boreal conditions over finland. Silva Fenn. 2010;44:213-33. https://doi.org/10.14214/sf.455

Lang ARG, Evans GN, Ho PY. Influence of local advection on evapotranspiration from irrigated rice in a semi-arid region. Agr Meteorol. 1974;13:5-13. https://doi.org/10.1016/0002-1571(74)90060-0

Li J, Li ZB, Guo MJ, Li P, Cheng SD, Yuan B. Effects of vegetation restoration on soil physical properties of abandoned farmland on the Loess Plateau, China. Environ Earth Sci. 2018;77:205-14. https://doi.org/10.1007/s12665-018-7385-7

Li XY, Liu LC, Duan ZH, Wang N. Spatio-temporal variability in remotely sensed surface soil moisture and its relationship with precipitation and evapotranspiration during the growing season in the Loess Plateau, China. Environ Earth Sci. 2014;71:1809-20. https://doi.org/10.1007/s12665-013-2585-7

Liancourt P, Sharkhuu A, Ariuntsetseg L, Boldgiv B, Helliker BR, Plante AF, Petraitis PS, Casper BB. Temporal and spatial variation in how vegetation alters the soil moisture response to climate manipulation. Plant Soil. 2012;351:249-61. https://doi.org/10.1007/s11104-011-0956-y

Liu Y, Li FL. A preliminary approach on the land surface temperature (LST) lapse rate of mountain area using MODIS data. In: Proceedings of the International Symposium of Remote Sensing and Space Technology for Multidisciplinary Research and Applications; 2005 May 19-24; Beijing, Peoples R China. Bellingham: Proceedings of SPIE; 2006. p. 7-15.

Liu Y, Qian JX, Yue H. Comparison and evaluation of different dryness indices based on vegetation indices-land surface temperature/albedo feature space. Adv Space Res-Series. 2021a;68:2791-803. https://doi.org/10.1016/j.asr.2021.05.007

Liu Y, Qian JX, Yue H. Comprehensive evaluation of Sentinel-2 Red Edge and shortwave-infrared bands to estimate soil moisture. IEEE J Sel Top Appl Earth Observ Remote Sens-Basel. 2021b;14:7448-65. https://doi.org/10.1109/jstars.2021.3098513

Liu YQ, Sha JM, Wang DS. Estimating the effects of DEM and land use types on soil moisture using HJ-1A CCD/IRS images: A case study in Minhou County. In: Proceedings of the 2nd International Conference on Energy and Environmental Protection (ICEEP 2013); 2013 Apr 19-21; Guilin, Peoples R China. Ann Arbor: University of Michigan Library; 2013. p. 4572-76.

Ma CY, Wang JL, Chen Z, Chen ZF, Liu ZD, Huang XQ. An assessment of surface soil moisture based on in situ observations and landsat 8 remote sensing data. Fresenius Environ Bull. 2017;26:6848-56.

Ma JZ, Pan YH, Gu CJ, Shu HP, Edmunds WM, Li D. Agricultural structure adjustment and ecosystem restoration planning at the village level to combat desertification: a pilot study in the Minqin Basin, Northwest China. In: Proceedings of the 3rd International Conference on Energy, Environment and Sustainable Development (EESD 2013); 2013 Nov 12-13; Shanghai, Peoples R China. State College: Pennsylvania State University; 2014. p. 2599-605.

Mallick J, Singh CK, Shashtri S, Rahman A, Mukherjee S. Land surface emissivity retrieval based on moisture index from LANDSAT TM satellite data over heterogeneous surfaces of Delhi city. Int J Appl Earth Obs. 2012;19:348-58. https://doi.org/10.1016/j.jag.2012.06.002

McAlary TA, Nicholson P, Groenevelt H, Bertrand D. A case study of soil-gas sampling in silt and clay-rich (low-permeability) soils. Ground Water Monit R. 2009;29:144-52. https://doi.org/10.1111/j.1745-6592.2009.01223.x

Mesbah SH, Kowsar SA. Spate irrigation of rangelands: a drought mitigating mechanism. In: Wager FC, editor. Nova science. Hauppauge: Nova Science Publishers, Inc; 2011. p. 39-78.

Mulder VL, Bruin S, Schaepman ME, Mayr TR. The use of remote sensing in soil and terrain mapping - A review. Geoderma. 2011;162:1-19. https://doi.org/10.1016/j.geoderma.2010.12.018

Ndossi MI, Avdan U. Application of open source coding technologies in the production of land surface temperature (LST) maps from landsat: a PyQGIS plugin. Remote Sens-Basel. 2016;8:413-44. https://doi.org/10.3390/rs8050413

Periasamy S, Shanmugam RS. Multispectral and microwave remote sensing models to survey soil moisture and salinity. Land Degrad Dev. 2017;28:1412-25. https://doi.org/10.1002/ldr.2661

Qi J, Chehbouni A, Huete AR, Kerr YH, Sorooshian S. A modified soil adjusted vegetation index. Remote Sens Environ. 1994;48:119-26. https://doi.org/10.1016/0034-4257(94)90134-1

Qin ZH, Li WJ, Gao MF, Zhang HO. Estimation of land surface emissivity for Landsat TM6 and its application to Lingxian Region in north China. In: Proceedings of the Conference on Remote Sensing for Environmental Monitoring, GIS Applications, and Geology VI; 2006 Sep 13-14; Stockholm, Sweden. Bellingham: Spie-Int Soc Optical Engineering; 2006. p. 7-18.

Ran Q, Zhang ZX, Zhou QB, Wang Q. Soil moisture derivation in China using AVHRR data and analysis of its affecting factors. In: Proceedings of the 25th IEEE International Geoscience and Remote Sensing Symposium (IGARSS 2005); 2005 Jul 25-29; Seoul, South Korea. New York: IEEE Xplore; 2005. p. 4497-500.

Ren HR, Zhou GS, Zhang F. Using negative soil adjustment factor in soil-adjusted vegetation index (SAVI) for aboveground living biomass estimation in arid grasslands. Remote Sens Environ. 2018;209:439-45. https://doi.org/10.1016/j.rse.2018.02.068

Ren XZ, Yang XP, Wang ZT, Zhu BQ, Zhang DG, Rioual P. Geochemical evidence of the sources of aeolian sands and their transport pathways in the Minqin Oasis, northwestern China. Quat Int. 2014;334:165-78. https://doi.org/10.1016/j.quaint.2014.04.037

Resources and Environment Science Center. Provincial DEM 30m data (SRTM 30m). Beijing,China: Resources and Environment Science Center; 2003. [cited 2021 Oct 21]. Available from: https://www.resdc.cn/data.aspx?DATAID=217

Sandholt I, Rasmussen K, Andersen J. A simple interpretation of the surface temperature/vegetation index space for assessment of surface moisture status. Remote Sens Environ. 2002;79:213-24. https://doi.org/10.1016/s0034-4257(01)00274-7

Seneviratne SI, Corti T, Davin EL, Hirschi M, Jaeger EB, Lehner I, Orlowsky B, Teuling AJ. Investigating soil moisture-climate interactions in a changing climate: A review. Earth-Sci Rev. 2010;99:125-61. https://doi.org/10.1016/j.earscirev.2010.02.004

Sousa MMM, Andrade EM, Palacio HAD, Medeiros PHA, Ribeiro JC. Spatial-temporal soil-water content dynamics in toposequences with different plant cover in a tropical semi-arid region. Rev Cienc Agron. 2022;53:e20217867. https://doi.org/10.5935/1806-6690.20220010

Sucksdorff Y, Ottle C. Application of satellite remote-sensing to estimate areal evapotranspiration over a watershed. J Hydrol. 1990;121:321-33. https://doi.org/10.1016/0022-1694(90)90238-s

Sun DF, Dawson R, Li BG. Agricultural causes of desertification risk in Minqin, China. J Environ Manage. 2006;79:348-56. https://doi.org/10.1016/j.jenvman.2005.08.004

Sun L, Wu Q, Pei ZY, Pan JW. study on the correlation between temperature vegetation dryness index (TVDI) and various factors. Geogr Geo-Inf Sci. 2010;26:31-4.

Sun YJ, Zheng XP, Qin QM, Meng QY, Gao ZL, Ren HZ, Wu L, Wang J, Wang JH. Modeling soil spectral reflectance with different mass moisture content. Spectrosc Spectr Anal. 2015;35:2236-40. https://doi.org/10.3964/j.issn.1000-0593(2015)08-2236-05

Thi DN, Ha NTT, Dang QT, Koike K, Trong NM. Effective band ratio of landsat 8 images based on VNIR-SWIR reflectance spectra of topsoils for soil moisture mapping in a tropical region. Remote Sens-Basel. 2019;11:716-34. https://doi.org/10.3390/rs11060716

Thieltges DW, Strasser M, Reise K. How bad are invaders in coastal waters? The case of the American slipper limpet crepidula fornicata in western Europe. Biol Invasions. 2006;8:1673-80. https://doi.org/10.1007/s10530-005-5279-6

United States Geological Survey. Landsat Collection 1 Level-1. South Dakota, American: Earth Resources Observation and Science (EROS); 2022 [cited 2021 Oct 18]. Available from: https://earth expiorer.usgs.gov/

Valor E, Caselles V. Mapping land surface emissivity from NDVI: Application to European, African, and south American areas. Remote Sens Environ. 1996;57:167-84. https://doi.org/10.1016/0034-4257(96)00039-9

Van Leeuwen WJD, Orr BJ, Marsh SE, Herrmann SM. Multi-sensor NDVI data continuity: Uncertainties and implications for vegetation monitoring applications. Remote Sens Environ. 2006;100:67-81. https://doi.org/10.1016/j.rse.2005.10.002

Wang H, He B, Zhang Y, Huang L, Chen Z, Liu J. Response of ecosystem productivity to dry/wet conditions indicated by different drought indices. Sci Total Environ. 2018;612:347-57. https://doi.org/10.1016/j.scitotenv.2017.08.212

Wang Y, Bolter M, Chang QR, Duttmann R, Marx K, Petersen JF, Wang ZL. Functional dependencies of soil CO_2 emissions on soil biological properties in northern German agricultural soils derived from a glacial till. Acta Agr Scand B-S P. 2015;65:233-45. https://doi.org/10.1080/09064710.2014.1000369

Wells NS, Gooddy DC, Reshid MY, Williams PJ, Smith AC, Eyre BD. δ^{18} O as a tracer of PO_4^{3-} losses from agricultural landscapes. J Environ Manage. 2022;317:115299. https://doi.org/10.1016/j.jenvman.2022.115299

Wigneron JP, Chanzy A, Calvet JC, Bruguier W. A simple algorithm to retrieve soil-moisture and vegetation biomass using passive microwave measurements over crop fields. Remote Sens Environ. 1995;51:331-41. https://doi.org/10.1016/0034-4257(94)00081-w

Wong EVS, Ward PR, Murphy DV, Leopold M, Barton L. Vacuum drying water-repellent sandy soil: Anoxic conditions retain original soil water repellency under variable soil drying temperature and air pressure. Geoderma. 2020;372:114385. https://doi.org/10.1016/j.geoderma.2020.114385

Wu CY, Deng L, Huang CB, Chen YF, Peng CH. Effects of vegetation restoration on soil nutrients, plant diversity, and its spatiotemporal heterogeneity in adesert-oasisecotone. Land Degrad Dev. 2021;32:670-83. https://doi.org/10.1002/ldr.3690

Wu FJ, Yu ZL, Wei XP, Deng JM, Li T, Zhao CM, Wang GX. Relationship between groundwater depth and pattern of net primary production in oasis-desert ecotone. Pol J Ecol. 2010;58:681-91.

Wu Z, Lei S, Bian Z, Huang J, Zhang Y. Study of the desertification index based on the albedo-MSAVI feature space for semi-arid steppe region. Environ Earth Sci. 2019;78:232-45. https://doi.org/10.1007/s12665-019-8111-9

Xiang MS, Deng QC, Duan LS, Yang J, Wang CJ, Liu JS, Liu ML. Dynamic monitoring and analysis of the earthquake Worst-hit area based on remote sensing. Alex Eng J. 2022;61:8691-702. https://doi.org/10.1016/j.aej.2022.02.001

Xie ZJ, Rosolem R. Impact of multi-day field calibration of novel cosmic-ray soil moisture sensors. In: Proceedings of the 16th IEEE Sensors Conference; 2017 Oct 29-Nov 01; Glasgow, Scotland. New York: IEEE Xplore; 2017. p. 1068-70.

Xu HX, Cao YG, Luo GB, Wang SF, Wang JM, Bai ZK. Variability in reconstructed soil bulk density of a high moisture content soil: a study on feature identification and ground penetrating radar detection. Environ Earth Sci. 2022;81:249. https://doi.org/10.1007/s12665-022-10365-1

Yan HB, Zhou G, Yang FF, Lu XJ. DEM correction to the TVDI method on drought monitoring in karst areas. Int J Remote Sens. 2019;40:2166-89. https://doi.org/10.1080/01431161.2018.1500732

Yang L, Wei W, Chen LD, Chen WL, Wang JL. Response of temporal variation of soil moisture to vegetation restoration in semi-arid Loess Plateau, China. Catena. 2014;115:123-33. https://doi.org/10.1016/j.catena.2013.12.005

Yang YG, Fu BJ. Soil water migration in the unsaturated zone of semiarid region in China from isotope evidence. Hydrol Earth Syst Sci. 2017;21:1757-67. https://doi.org/10.5194/hess-21-1757-2017

Youhao E, Jihe W, Shangyu G, Ping Y, Zihui Y. Monitoring of vegetation changes using multi-temporal NDVI in peripheral regions around Minqin oasis, Northwest China. In: Proceedings of the IEEE International Geoscience and Remote Sensing Symposium (IGARSS); 2007 Jul 23-27; Barcelona, Spain. New York: IEEE Xplore; 2007. p. 34-48.

Yuan LN, Li L, Zhang T, Chen LQ, Zhao JL, Hu S, Cheng L, Liu WQ. Soil moisture estimation for the chinese loess plateau using MODIS-derived ATI and TVDI. Remote Sens-Basel. 2020;12:35. https://doi.org/10.3390/rs12183040

Zhang DJ, Tang RL, Zhao W, Tang BH, Wu H, Shao K, Li ZL. Surface soil water content estimation from thermal remote sensing based on the temporal variation of land surface temperature. Remote Sens-Basel. 2014a;6:3170-87. https://doi.org/10.3390/rs6043170

Zhang KC, Qu JJ, Liu QH. Environmental degradation in the minqin oasis in northwest china during recent 50 years. J Environ Syst. 2004;31:357-65. https://doi.org/10.2190/ES.31.4.e

Zhang LF, Jiao WZ, Zhang HM, Huang CP, Tong QX. Studying drought phenomena in the Continental United States in 2011 and 2012 using various drought indices. Remote Sens Environ. 2017;190:96-106. https://doi.org/10.1016/j.rse.2016.12.010

Zhang Q, Li JF, Gu XH, Shi PJ. Is the pearl river basin, China, drying or wetting? Seasonal variations, causes and implications. Global Planet Change. 2018;166:48-61. https://doi.org/10.1016/j.gloplacha.2018.04.005

Zhang X, Ding F, Peng XL, Wu WF, Fan PY. Fast retrieval of land surface emissivity from landsat data through IDL programming. In: Proceedings of the 3rd International Workshop on Earth Observation and Remote Sensing Applications (EORSA); 2014 Jun 11-14; Changsha, Peoples R China. New York: IEEE Xplore; 2014b. p. 76-80.

Zhao HF, He HM, Wang JJ, Bai CY, Zhang CJ. Vegetation restoration and its environmental effects on the loess plateau. Sustainability-basel. 2018;10:4676. https://doi.org/10.3390/su10124676

Zhao X, Huang N, Song XF, Li ZY, Niu Z. A new method for soil moisture inversion in vegetation-covered area based on Radarsat 2 and Landsat 8. J Infrared Millim W. 2016;35:609-16. https://doi.org/10.11972/j.issn.1001-9014.2016.05.016

Zhen ZJ, Chen SB, Yin TG, Chavanon E, Lauret N, Guilleux J, Henke M, Qin WH, Cao LS, Li J, Lu P, Gastellu-Etchegorry JP. using the negative soil adjustment factor of soil adjusted vegetation index (SAVI) to resist saturation effects and estimate leaf area index (LAI) in dense vegetation areas. Sensors. 2021;21:2115. https://doi.org/10.3390/s21062115

Zheng PF, Wang DD, Yu XX, Jia GD, Liu ZQ, Wang YS, Zhang YG. Effects of drought and rainfall events on soil autotrophic respiration and heterotrophic respiration. Agric Ecosyst Environ. 2021;308:107267. https://doi.org/10.1016/j.agee.2020.107267

Zhou P, Wen AB, Zhang XB, He XB. Soil conservation and sustainable eco-environment in the Loess Plateau of China. Environ Earth Sci. 2013;68:633-9. https://doi.org/10.1007/s12665-012-1766-0